

# **An empirical algorithm to map perennial firn aquifers and ice slabs within the Greenland Ice Sheet using satellite L-band microwave radiometry**

Julie Z. Miller<sup>1,2</sup>, Riley Culberg<sup>3</sup>, David G. Long<sup>4</sup>, Christopher A. Shuman<sup>5</sup>,  
Dustin M. Schroeder<sup>3,6</sup>, Mary J. Brodzik<sup>1,7</sup>

<sup>1</sup>Cooperative Institute for Research in Environmental Sciences, University of Colorado, Boulder, Colorado, USA

<sup>2</sup>Earth Science and Observation Center, University of Colorado, Boulder, Colorado, USA

<sup>3</sup>Department of Electrical Engineering, Stanford University, Stanford, California, USA

<sup>4</sup>Department of Electrical and Computer Engineering, Brigham Young University, Provo, Utah, USA

<sup>5</sup>University of Maryland, Baltimore County, Joint Center for Earth Systems Technology at Code 615,  
Cryospheric Sciences Laboratory NASA Goddard Space Flight Center, Greenbelt, Maryland, USA

<sup>6</sup>Department of Geophysics, Stanford University, Stanford, CA, USA

<sup>7</sup>National Snow and Ice Data Center, University of Colorado, Boulder, Colorado, USA

**Correspondence to:** jzmiller.research@gmail.com

## **Abstract**

*Perennial firn aquifers are subsurface meltwater reservoirs consisting of a meters-thick water-saturated firn layer that can form on spatial scales as large as tens of kilometers. They have been observed within the percolation facies of glaciated regions experiencing intense seasonal surface melting and high snow accumulation. Widespread perennial firn aquifers have been identified within the Greenland Ice Sheet (GrIS) via field expeditions, airborne ice-penetrating radar surveys, and satellite microwave sensors. In contrast, ice slabs are nearly-continuous ice layers that can also form on spatial scales as large as tens of kilometers as a result of surface and subsurface water-saturated snow and firn layers sequentially refreezing following multiple melting seasons. They have been observed within the percolation facies of glaciated regions experiencing intense seasonal surface melting, but in areas where snow accumulation is at least 25% lower as compared to perennial firn aquifer areas. Widespread ice slabs have recently been identified within the GrIS via field expeditions and airborne ice-penetrating radar surveys, specifically in areas where perennial firn aquifers typically do not form. However, ice slabs have yet to be identified from space. Together, these two ice sheet features represent distinct, but related, sub-facies within the broader percolation facies of the GrIS that can be defined primarily by differences in snow accumulation, which influences the englacial hydrology and thermal characteristics of firn layers at depth.*

*Here, for the first time, we use enhanced-resolution vertically-polarized L-band brightness temperature ( $T_V^B$ ) imagery (2015-2019) generated using observations collected over the GrIS by NASA's Soil Moisture Active Passive (SMAP) satellite to map perennial firn aquifer and ice slab areas together as a continuous englacial hydrological system. We use an empirical algorithm previously developed to map the extent of Greenland's perennial firn aquifers via fitting exponentially decreasing temporal L-band signatures to a set of sigmoidal curves. This algorithm is recalibrated to also map the extent of ice slab areas using airborne ice-penetrating radar surveys collected by NASA's Operation Ice Bridge (OIB) campaigns (2010-2017). Our SMAP-derived maps*

41 *show that between 2015 and 2019, perennial firn aquifer areas extended over 64,000 km<sup>2</sup>, and ice*  
42 *slab areas extended over 76,000 km<sup>2</sup>. Combined together, these sub-facies are the equivalent of*  
43 *24% of the percolation facies of the GrIS. As Greenland's climate continues to warm, seasonal*  
44 *surface melting will increase in extent, intensity, and duration. Quantifying the possible rapid*  
45 *expansion of these sub-facies using satellite L-band microwave radiometry has significant*  
46 *implications for understanding ice sheet-wide variability in englacial firn hydrology that may drive*  
47 *meltwater-induced hydrofracturing and accelerated ice flow as well as high-elevation meltwater*  
48 *runoff that can impact the mass balance and stability of the GrIS.*

## 49 **1 Introduction**

50 The recent launches of several satellite L-band microwave radiometry missions by NASA (Aquarius  
51 mission, Levine, et al., 2007; Soil Moisture Active Passive (SMAP) mission, Entekhabi et al., 2010) and  
52 ESA (Soil Moisture and Ocean Salinity (SMOS), Kerr et al., 2010) have provided a new Earth-observation  
53 tool capable of detecting meltwater stored tens of meters to kilometers beneath the ice sheet surface. Jezek  
54 et al. (2015) recently demonstrated that in the high-elevation (3500 m a.s.l.) dry snow facies of the Antarctic  
55 Ice Sheet, meltwater stored in subglacial Lake Vostok can be detected as deep as 4 km beneath the ice  
56 sheet surface. Subglacial lakes represent radiometrically cold subsurface meltwater reservoirs. Upwelling  
57 L-band emission from the radiometrically warm bedrock underlying the subglacial lakes is effectively  
58 blocked by high reflectivity and attenuation at the interface between the bedrock and the overlying lake  
59 bottom. This results in a lower observed microwave brightness temperature ( $T^B$ ) at the ice sheet surface  
60 as compared to other dry snow facies areas where bedrock contributes to L-band emission depth-integrated  
61 over the entire ice sheet thickness.

62 Similar to subglacial lakes, perennial firn aquifers also represent radiometrically cold subsurface  
63 meltwater reservoirs (Miller et al., 2020) consisting of a 4-25 m thick water-saturated firn layer (Koenig et  
64 al., 2014; Montgomery et al., 2017; Chu et al., 2018) that can form on spatial scales as large as tens of  
65 kilometers (Forster et al., 2014). Perennial firn aquifers have been identified via field expeditions (Forster  
66 et al., 2014), airborne ice-penetrating radar surveys (Miège et al., 2016), and satellite microwave sensors  
67 (Brangers et al., 2020; Miller et al., 2020) in the lower-elevation (<2000 m a.s.l.) percolation facies of the  
68 Greenland Ice Sheet (GrIS) at depths from between 1 m and 40 m beneath the ice sheet surface. They  
69 exist in areas that experience intense seasonal surface melting and rain (>650 mm w.e. yr<sup>-1</sup>) during the  
70 melting season and high snow accumulation (>800 mm w.e. yr<sup>-1</sup>) during the freezing season (Forster et al.,  
71 2014). High snow accumulation in perennial firn aquifer areas thermally insulates water-saturated firn layers  
72 from the cold atmosphere allowing seasonal meltwater to be stored in liquid form year-round if the overlying  
73 seasonal snow layer is sufficiently thick (Kuipers Munneke et al., 2014). Koenig et al. (2014) estimated that  
74 the volumetric fraction of meltwater stored within the pore space of Greenland's perennial firn aquifers just  
75 prior to melt onset ranges from between 10% and 25%, which limits the upward propagation of  
76 electromagnetic energy from greater depths within the ice sheet. Large volumetric fractions of meltwater  
77 within the firn pore space results in high reflectivity and attenuation at the interface between water-saturated

78 firn layers and the overlying refrozen firn layers, and between glacial ice or an impermeable layer and the  
79 overlying water-saturated firn layers. Upwelling L-band emission from deeper glacial ice and the underlying  
80 bedrock is effectively blocked.

81 While perennial firn aquifers are radiometrically cold, the slow refreezing of deeper firn layers  
82 saturated with large volumetric fractions of meltwater represents a significant source of latent heat that is  
83 continuously released throughout the freezing season. Refreezing of seasonal meltwater by the descending  
84 winter cold wave (Pfeffer et al., 1991), and the subsequent formation of embedded ice structures (i.e.,  
85 horizontally-oriented ice layers and ice lenses, and vertically-oriented ice pipes; Benson et al., 1960;  
86 Humphrey et al., 2012; Harper et al., 2012) within the upper snow and firn layers represents a secondary  
87 source of latent heat. These heat sources help maintain meltwater at depth. Perennial firn aquifer areas  
88 are radiometrically warmer than other percolation facies areas where the single source of latent heat is via  
89 refreezing of seasonal meltwater. This results in a higher observed  $T^B$  at the ice sheet surface during the  
90 freezing season as compared to other percolation facies areas where seasonal meltwater is fully refrozen  
91 and stored exclusively as embedded ice.

92 Recently, mapping the extent of Greenland's perennial firn aquifers from space was demonstrated  
93 using satellite L-band microwave radiometry (Miller et al., 2020). Exponentially decreasing temporal L-band  
94 signatures observed in enhanced-resolution vertically-polarized L-band brightness temperature ( $T_V^B$ )  
95 imagery (2015-2016) generated using observations collected over the GrIS by the microwave radiometer  
96 on NASA's SMAP satellite (Long et al., 2019) were correlated with a single year of perennial firn aquifer  
97 detections (Miège et al. 2016). These detections were identified via the Center for Remote Sensing of Ice  
98 Sheets (CReSIS) Multi-Channel Coherent Radar Depth Sounder (MCoRDS) flown by NASA's Operation  
99 Ice Bridge (OIB) campaigns (Rodriguez-Morales et al, 2014). An empirical algorithm to map extent was  
100 developed by fitting temporal L-band signatures to a set of sigmoidal curves derived from the continuous  
101 logistic model.

102 The relationship between the radiometric, and thus the physical, temperature of perennial firn  
103 aquifer areas, as compared to other percolation facies areas, forms the basis of the empirical algorithm.  
104 Miller et al. (2020) hypothesized that the dominant control on the relatively slow exponential rate of  $T^B$   
105 decrease over perennial firn aquifer areas is physical temperature versus depth. L-band emission from the  
106 radiometrically warm upper snow and firn layers decreases during the freezing season as embedded ice  
107 structures slowly refreeze at increased depths below the ice sheet surface. In the percolation facies,  
108 refreezing of seasonal meltwater results in the formation of an intricate network of embedded ice structures  
109 that are large (10-100 cm long, 10-20 cm wide; Jezek et al., 1994) relative to the L-band wavelength (21  
110 cm). Embedded ice structures induce strong volume scattering (Rignot et al., 1993; Rignot 1995) that  
111 decreases  $T^B$  (Zwally, 1977; Swift et al. 1985; Jezek et al., 2018).

112 Ice slabs are 1-16 m thick nearly-continuous ice layers that that can form on spatial scales as large  
113 as tens of kilometers as a result of surface and subsurface water-saturated snow and firn layers sequentially  
114 refreezing following multiple melting seasons (Machguth et al., 2016; MacFerrin et al., 2019). Over time,

115 they become dense low-permeability solid-ice layers overlying deeper permeable firn layers. Ice slabs have  
116 been identified via field expeditions and airborne ice-penetrating radar surveys in the lower-elevation  
117 (<2000 m a.s.l.) percolation facies of the GrIS at depths from between 1 m and 20 m beneath the ice sheet  
118 surface (MacFerrin et al., 2019). They exist in areas that experience intense seasonal surface melting and  
119 rain (excess melt of 266-573 mm w.e. yr<sup>-1</sup>, see MacFerrin et al., (2019) for a description) during the melting  
120 season, and lower snow accumulation (<572+/-32 mm w.e. yr<sup>-1</sup>) during the freezing season as compared  
121 to perennial firn aquifer areas (MacFerrin et al., 2019). Lower snow accumulation in ice slab areas results  
122 in a seasonal snow layer that is insufficiently thick to thermally insulate water-saturated firn layers and  
123 seasonal meltwater is instead stored as embedded ice. Refreezing of seasonal meltwater by the  
124 descending winter cold wave, and the subsequent formation of ice slabs as well as other embedded ice  
125 structures within the upper snow and firn layers is the single source of latent heat. While ice slab areas are  
126 radiometrically warmer than other percolation facies areas with a lower volumetric fraction of embedded  
127 ice, they are radiometrically colder than perennial firn aquifer areas. This results in typically higher observed  
128  $T^B$  at the ice sheet surface during the freezing season in ice slab areas, as compared to other percolation  
129 facies areas, however, typically lower observed  $T^B$  as compared to perennial firn aquifer areas. Similar to  
130 temporal L-band signatures over perennial firn aquifer areas, temporal L-band signatures over ice slab  
131 areas are exponentially decreasing during the freezing season, however, the rate of  $T^B$  decrease is slightly  
132 more rapid.

133 In this study, we exploit the observed sensitivity of L-band emission to differences in the depth- and  
134 time-integrated dielectric and geophysical properties of the percolation facies of the GrIS to map perennial  
135 firn aquifer and ice slab areas together as a continuous englacial firn hydrological system using satellite L-  
136 band microwave radiometry.

## 137 **2 Methods**

138 We adapt our previously developed empirical algorithm to map the extent of Greenland's perennial firn  
139 aquifers (Miller et al., 2020) using a multi-year calibration technique. We use enhanced-resolution L-band  
140  $T_V^B$  imagery (2015-2019) generated using observations collected over the GrIS by the microwave  
141 radiometer on NASA's SMAP satellite (Long et al., 2019) and airborne ice-penetrating radar surveys  
142 collected by NASA's OIB campaigns (Rodriguez-Morales et al, 2014). First, we correlate: (1) a 'firn  
143 saturation' parameter derived from a simple two-layer L-band brightness temperature model (Miller et al.,  
144 2021, in press), (2) maximum and (3) minimum  $T_V^B$  values, and (4) exponentially decreasing temporal L-  
145 band signatures, with five years of perennial firn aquifer detections (2010-2014) identified via the CReSIS  
146 Accumulation Radar (AR) (Miège et al. 2016), and three years of additional detections (2015-2017) more  
147 recently identified via MCoRDS (Miller et al., 2020). Next, we extend our empirical algorithm to map the  
148 extent of ice slab areas. We correlate the SMAP-derived parameters with five years of ice slab detections  
149 (2010-2014) recently identified via AR (MacFerrin et al., 2019). Finally, we re-calibrate our empirical model  
150 to map the extent of perennial firn aquifer and ice slab areas over the percolation facies. Interannual

151 variability in extent is not resolved in this study, however, it will be explored further in future work.

## 152 **2.1 SMAP Enhanced-Resolution L-band $T^B$ Imagery**

153 The key science objectives of NASA's SMAP mission (<https://smap.jpl.nasa.gov/>) are to map terrestrial soil  
154 moisture and freeze/thaw state over Earth's land surfaces from space. However, the global L-band  $T^B$   
155 observations collected by the SMAP satellite also have cryospheric applications. Mapping perennial firn  
156 aquifer and ice slab areas over Earth's polar ice sheets represents an interesting analog and an innovative  
157 extension of the [SMAP mission's](#) science objectives. The SMAP satellite was launched 31 January 2015  
158 and carries a microwave radiometer that operates at an L-band frequency of 1.41 GHz (Enkentabi et al.,  
159 2010). It is currently collecting observations of vertically and horizontally-polarized  $T^B$  over Greenland. The  
160 surface incidence angle is  $40^\circ$ , and the radiometric accuracy is approximately 1.3 K (Piepmeier et al., 2017).

161 The Scatterometer Image Reconstruction (SIR) algorithm was originally developed to reconstruct  
162 coarse resolution satellite radar scatterometry imagery on a higher spatial resolution grid (Long et al., 1993;  
163 Early and Long, 2001). The SIR algorithm has been adapted for coarse resolution satellite microwave  
164 radiometry imagery (Long and Daum, 1998; Long and Brodzik, 2016; Long et al., 2019). The microwave  
165 radiometer form of the SIR algorithm (rSIR) uses the measurement response function (MRF) for each  
166 observation, which is a smeared version of the antenna pattern. Using the overlapping MRFs, the rSIR  
167 algorithm reconstructs  $T^B$  from the spatially filtered low-resolution sampling provided by the observations.  
168 In effect, it generates an MRF-deconvolved  $T^B$  image. Combining multiple orbital passes increases the  
169 sampling density, which improves both the accuracy and resolution of the SMAP enhanced-resolution  $T^B$   
170 imagery (Long et al., 2019).

171 Over Greenland, the rSIR algorithm combines satellite orbital passes that occur between 8 a.m.  
172 and 4 p.m. local time-of-day to reconstruct SMAP enhanced-resolution  $T^B$  imagery twice-daily (i.e., morning  
173 and evening orbital pass interval, respectively).  $T^B$  imagery is projected on a Northern Hemisphere (NH)  
174 Equal-Area Scalable Earth Grid (EASE-Grid 2.0; Brodzik et al., 2012) at a 3.125 km rSIR grid cell spacing  
175 (e.g., Fig. 1). The effective resolution for each grid cell is dependent on the number of observations used  
176 in the rSIR reconstruction and is coarser than the rSIR grid cell spacing. While the effective resolution of  
177 conventionally processed SMAP  $T^B$  imagery posted on a 25 km grid is approximately 30 km (e.g., Fig. 1a),  
178 the effective resolution of SMAP enhanced-resolution  $T^B$  imagery posted on a 3.125 km grid is  
179 approximately 18 km (e.g., Fig. 1b), an improvement of 60% (Long et al., 2020).

180 As previously noted, for our analysis of the percolation facies we use SMAP enhanced-resolution  
181  $T_V^B$  imagery over the GrIS. Compared to the horizontally-polarized channel, the vertically-polarized channel  
182 exhibits decreased sensitivity to variability in the volumetric fraction of meltwater, which is attributed to  
183 reflection coefficient differences between channels (Miller et al., 2020). Using the vertically polarized  
184 channel also results in a reduced chi-squared error statistic when fitting  $T_V^B$  time series to the sigmoid  
185 function (Section 2.3.4). We construct  $T_V^B$  imagery that alternate morning and evening orbital pass  
186 observations annually, beginning and ending just prior to melt onset. The Greenland Ice Mapping Project

187 (GIMP) Land Ice and Ocean Classification Mask and Digital Elevation Model (Howat et al., 2014) are  
188 projected on the NH EASE-Grid 2.0 at a 3.125 km rSIR grid cell spacing. The derived ice mask includes  
189 the Greenland Ice Sheet and the peripheral ice caps, including Maniitsoq and Flade Isblink.  $T_V^B$  imagery  
190 between 1 April 2015 and 31 March 2019 are ice ~~sheet~~-masked, and an elevation for each rSIR grid cell is  
191 calculated.

## 192 **2.2 Airborne Ice-Penetrating Radar Surveys**

193 AR and MCoRDS (Rodriguez-Morales et al, 2014) were flown over the GrIS on a P-3 aircraft in  
194 April and May between 2010 and 2017. The AR instrument operates at a center frequency of 750 MHz with  
195 a bandwidth of 300 MHz, resulting in a range resolution in firm of 0.53 m (Lewis et al., 2015). The collected  
196 data have an along-track resolution of approximately 30 m with 15 m spacing between traces in the final  
197 processed radargrams. At a nominal flight altitude of 500 m above the ice sheet surface, the cross-track  
198 resolution varies between 20 m for a smooth surface, to 54 m for a rough surface with no appreciable  
199 layover. The MCoRDS instrument operated at three different frequency configurations: (1) a center  
200 frequency of 195 MHz with a bandwidth of 30 MHz (2010-2014, 2017, 2018), (2) a center frequency of 315  
201 MHz with a band width of 270 MHz (2015), and (3) a center frequency of 300 MHz with a bandwidth of 300  
202 MHz (2016). The vertical range resolution in firm for each of these frequency configurations is 5.3 m, 0.59  
203 m, and 0.53m, respectively (CReSIS, 2016). The collected data have an along-track resolution of  
204 approximately 25 m with 14 m spacing between traces in the final processed radargrams. At the same  
205 nominal flight altitude of 500 m, the cross-track resolution varies between 40 m for a smooth surface in the  
206 highest bandwidth configuration, to 175 m for a rough surface with no appreciable layover in the lowest  
207 bandwidth configuration.

208 The multi-year calibration technique uses perennial firm aquifer detections previously identified  
209 along OIB flight lines via AR (2010-2014) and MCoRDS (2015-2017) radargram profiles and the  
210 methodology described in Miège et al. (2016). Bright lower reflectors that undulate with the local  
211 topographic gradient underneath which reflectors are absent in the percolation facies are interpreted as the  
212 upper surface of meltwater stored within perennial firm aquifers (e.g., Fig. 3a). The large dielectric contrast  
213 between refrozen and water-saturated firm layers results in high reflectivity at the interface. However, the  
214 presence of meltwater increases attenuation, limiting the downward propagation of electromagnetic energy  
215 through the water-saturated firm layer. The total number of AR derived perennial firm aquifer detections is  
216 325,000, corresponding to a total extent of 98 km<sup>2</sup>. The analysis assumes a smooth surface, which is typical  
217 of much of the percolation facies, and a grid cell size of 15 m x 20 m. The total number of MCoRDS-derived  
218 perennial firm aquifer detections is 142,000, corresponding to a total extent of 80 km<sup>2</sup>. This analysis also  
219 assumes a smooth surface, and a grid cell size of 14 m x 40 m. The combined total number of grid cells  
220 (467,000) and total extent (178 km<sup>2</sup>) is significantly larger than the total number of MCoRDS-derived grid  
221 cells (78,000) and total extent (44 km<sup>2</sup>) calculated for 2016 (Miller et al., 2020). Perennial firm aquifer  
222 detections are mapped in north western, southern, and south and central eastern Greenland as well as the

223 Maniitsoq and Flade Isblink Ice Caps (Figs. 1c; 2a). We project AR- and MCoRDS-derived perennial firn  
224 aquifer detections on the NH EASE-Grid 2.0 at an rSIR grid cell spacing of 3.125 km. Each rSIR grid cell  
225 has an extent of approximately 10 km<sup>2</sup>. The total number of rSIR grid cells with at least one perennial firn  
226 aquifer detection is 800, corresponding to a total extent of 8000 km<sup>2</sup>. However, given the limited AR and  
227 MCoRDS grid cell coverage, less than 1% of the rSIR grid cell extent has airborne ice-penetrating radar  
228 survey coverage. As compared to the total number of MCoRDS-derived perennial firn aquifer detections  
229 (780) calculated for 2016 (Miller et al., 2020), the total number of rSIR grid cells with at least one detection  
230 is only increased by 20 for the multi-year calibration technique, corresponding to an increased total extent  
231 of 200 km<sup>2</sup>.

232 We also use ice slab detections previously identified along OIB flight lines via AR (2010-2014)  
233 radargram profiles and the methodology described in MacFerrin et al. (2019) in the multi-year calibration  
234 technique. Thick dark surface-parallel regions of low-reflectivity in the percolation facies are interpreted as  
235 ice slabs (e.g., Fig. 3b). The large dielectric contrast between ice slabs and the overlying and underlying  
236 snow and firn layers results in high reflectivity at the interfaces. However, electromagnetic energy is not  
237 scattered or absorbed within the homogeneous ice slab, it instead propagates downward through the layer  
238 and into the deeper firn layers. The total number of AR-derived ice slab detections is 505,000,  
239 corresponding to a total extent of 283 km<sup>2</sup>. Ice slab detections are mapped in western, central and north  
240 eastern, and northern Greenland as well as the Flade Isblink Ice Cap (Figs. 1c; 2b). We project the AR-  
241 derived ice slab detections on the NH EASE-Grid 2.0 at an rSIR grid cell spacing of 3.125 km. The total  
242 number of rSIR grid cells with at least one ice slab detection is 2000, corresponding to a total extent of  
243 20,000 km<sup>2</sup>. However, less than 2% of the rSIR grid cell extent has airborne ice-penetrating radar survey  
244 coverage.

245 An advantage of the multi-year calibration technique as compared to the single-coincident year  
246 calibration technique (Miller et al., 2020) is that it increases the number of rSIR grid cells that can be  
247 assessed. It also provides repeat targets that can account for variability in the depth- and time-integrated  
248 dielectric and geophysical properties that influence the radiometric temperature in stable perennial firn  
249 aquifer and ice slab areas. Uncertainty is introduced by correlating the SMAP-derived parameters with AR-  
250 and MCoRDS-derived detections that are not coincident in time. The multi-year calibration technique  
251 assumes the extent of each area remains stable, which is not necessarily the case as climate extremes  
252 (Cullather et al., 2020) can influence each of these sub-facies. The assumption of stability neglects  
253 boundary transitions in the extent of perennial firn aquifer areas associated with refreezing of shallow water-  
254 saturated firn layers, englacial drainage of meltwater into crevasses at the periphery (Poinar et al., 2017;  
255 Poinar et al, 2019), and transient upslope expansion (Montgomery et al., 2017). Once formed, ice slabs are  
256 essentially permanent features within the upper snow and firn layers of the percolation facies until they are  
257 compressed into glacial ice. However, they may transition into superimposed ice at the lower boundary of  
258 ice slab areas or rapidly expand upslope, particularly following extreme melting seasons (MacFerrin et al.,  
259 2019). Thus, we simply consider our mapped extent a high-probability area for the preferential formation of

260 each of these sub-facies, with continued presence dependent on seasonal surface melting and snow  
261 accumulation in subsequent years.

262 Annual perennial firn aquifer and ice slab detections that may introduce significant uncertainty into  
263 the multi-year calibration technique include those following the 2010 melting season, which was  
264 exceptionally long (Tedesco et al., 2011), the anomalous 2012 melting season, during which seasonal  
265 surface melting extended across 99% of the GrIS (Nghiem et al., 2012), and the 2015 melting season,  
266 which was especially intense in western and northern Greenland (Tedesco et al., 2016). Following these  
267 extreme melting seasons, significant changes in the dielectric and geophysical properties likely occurred  
268 across large portions of the GrIS, including perennial firn aquifer recharging resulting in increases in  
269 meltwater volume and decreases in the depth to the upper surface of stored meltwater. The upper snow  
270 and firn layers of the dry snow facies and percolation facies were also saturated with relatively large  
271 volumetric fractions of meltwater as compared to the negligible to limited volumetric fractions of meltwater  
272 that percolates during more typical seasonal surface melting on the GrIS.

273 Seasonal meltwater was refrozen into spatially coherent melt layers following the 2010 and 2012  
274 melting seasons (Culberg et al., 2021) as well as more recently following the 2015, and 2018 melting  
275 seasons identified as part of the temporal L-band signature analysis in this study (Section 2.3.1). As  
276 compared to ice slabs, which are dense low-permeability solid-ice layers, spatially coherent melt layers are  
277 a network of embedded ice structures primarily consisting of discontinuous horizontally-oriented ice layers  
278 and ice lenses sparsely connected via vertical-oriented ice pipes (Culberg et al., 2021). Spatially coherent  
279 melt layers are relatively thin (0.2 cm-2 m) and can rapidly form across the high-elevation (up to 3200 m  
280 a.s.l.) dry snow facies at depths of less than 1 m beneath the ice sheet surface following a single extreme  
281 melting season. They can further merge together into thicker solid-ice layers following multiple extreme  
282 melting seasons. Spatially coherent melt layers are exceptionally bright in AR radargrams (e.g., Fig 3a).  
283 The large dielectric contrast between the spatially coherent melt layer and the overlying, underlying, and  
284 interior snow and firn layers results in high reflectivity at the interfaces. However, electromagnetic energy  
285 still propagates downward through the high reflectivity layer into the deeper firn layers. Culberg et al., (2021)  
286 recently demonstrated mapping the extent of spatially coherent melt layers formed following the 2012  
287 melting season (Nghiem et al., 2012) via AR (Figs. 1c; 2).

## 288 **2.3 Empirical Algorithm**

### 289 **2.3.1 Temporal L-band Signatures over the Percolation Facies**

290  $T^B$  expresses the satellite-observed magnitude of thermal emission and is influenced by the microwave  
291 instrument's observation geometry as well as the depth- and time-integrated dielectric and geophysical  
292 properties of the ice sheet (Ulaby et al., 2014). The most significant geophysical property influencing  $T^B$  is  
293 the volumetric fraction of meltwater within the snow and firn pore space (Mätzler and Hüppli, 1989). During  
294 the melting season, the upper snow and firn layers of the percolation facies are saturated with large  
295 volumetric fractions of meltwater that percolates vertically into the deeper firn layers (Benson, 1960;



296 Humphrey et al., 2012). Increases in the volumetric fraction of meltwater results in rapid relative increases  
297 in the imaginary part of the complex dielectric constant (Tiuri et al., 1984). This typically increases  $T^B$ , and  
298 decreases volume scattering and penetration depth. The L-band penetration depth can rapidly decrease  
299 from tens to hundreds of meters to less than a meter, dependent on the local snow and firn conditions.  
300 During the freezing season, surface and subsurface water-saturated snow and firn layers and embedded  
301 ice structures subsequently refreeze. Decreases in the volumetric fraction of meltwater results in rapid  
302 relative decreases in the imaginary part of the complex dielectric constant. This decreases  $T^B$ , and  
303 increases volume scattering and penetration depth. The L-band penetration depth increases back to tens  
304 to hundreds of meters on variable time scales.

305 We analyze melting and freezing seasons in temporal L-band signatures exhibited in  $T_V^B$  time series  
306 over and near the AR- and MCoRDS-derived perennial firn aquifer and ice slab detections projected on the  
307 NH EASE-Grid 2.0 (Fig. 4; Table 1). We project ice surface temperature observations calculated using  
308 thermal infrared brightness temperature collected by the Moderate Resolution Imaging Spectroradiometer  
309 (MODIS) on the Terra and Aqua satellites (Hall et al., 2012) on the NH EASE-Grid 2.0 at a 3.125 km rSIR  
310 grid cell spacing. We then derive melt onset and surface freeze-up dates for each rSIR grid cell using the  
311 methodology described in Miller et al., (2020). We set a threshold of ice surface temperature  $>-1^\circ\text{C}$  for  
312 meltwater detection (Nghiem et al., 2012), consistent with the  $\pm 1^\circ\text{C}$  accuracy of the ice surface temperature  
313 observations. For temperatures that are close to  $0^\circ\text{C}$ , ice surface temperatures are closely compatible with  
314 contemporaneous NOAA near-surface air temperature observations (Shuman et al., 2014). Melt onset and  
315 surface freeze-up dates are overlaid on  $T_V^B$  time series to partition the melting and freezing seasons. Melt  
316 onset dates typically occur between April and July, and surface freeze-up dates typically occur between  
317 July and September. The melting season increases in duration moving downslope from the dry snow facies,  
318 and ranges from a single day in the highest elevations ( $>2500$  m) of the percolation facies, to 150 days in  
319 the ablation facies. Similarly, the freezing season decreases in duration moving downslope, and ranges  
320 from between 215 days and 365 days.

321 Over perennial firn aquifer areas (e.g., Fig. 4a, SMAP Test Site A:  $66.2115^\circ\text{N}$ ,  $39.1795^\circ\text{W}$ , 1625 m  
322 a.s.l.), maximum  $T_V^B$  ( $T_{V,max}^B$ ) values are radiometrically warm during the melting season. Vertically  
323 percolating meltwater and gravity-driven meltwater drainage seasonally recharges perennial firn aquifers  
324 at depth (Fountain and Walder et al., 1998). Minimum  $T_V^B$  ( $T_{V,min}^B$ ) values remain radiometrically warm during  
325 the freezing season as a result of latent heat continuously released by the slow refreezing of the deeper  
326 firn layers that are saturated with large volumetric fractions of meltwater (Miller et al, 2020). Temporal L-  
327 band signatures exhibit slow exponential decreases and approach, and sometimes achieve, stable  $T_V^B$   
328 values.  $T_V^B$  can decrease by more than 50 K during the freezing season, which represents the descent of  
329 the upper surface of stored meltwater by depths of meters to tens of meters beneath the ice sheet surface  
330 (Miège et al., 2016).

331 Over ice slab areas (e.g., Fig. 4b, SMAP Test Site B:  $66.8850^\circ\text{N}$ ,  $42.7765^\circ\text{W}$ , 1817 m a.s.l.),  $T_{V,max}^B$   
332 values are typically radiometrically colder than over perennial firn aquifer areas during the melting season.

333 The presence of dense low-permeability solid-ice layers reduces the snow and firn pore space available to  
334 store seasonal meltwater at depth. Meltwater may alternatively runoff ice slabs downslope towards the wet  
335 snow facies.  $T_{V,min}^B$  values are also typically radiometrically colder than over perennial firn aquifer areas  
336 during the freezing season as a result of the absence of meltwater stored at depth. Temporal L-band  
337 signatures exhibit exponential decreases that are slightly more rapid than over perennial firn aquifer areas,  
338 and often achieve stable  $T_V^B$  values.

339 Over other percolation facies areas (e.g., Fig. 4c, SMAP Test Site C: 66.9024°N, 44.7528°W, 2350  
340 m a.s.l.), where seasonal meltwater is fully refrozen and stored exclusively as embedded ice,  $T_{V,max}^B$  values  
341 are typically radiometrically colder than over perennial firn aquifer and ice slab areas during the melting  
342 season.  $T_{V,min}^B$  values are also typically radiometrically cold during the freezing season. Temporal L-band  
343 signatures exhibit rapid exponential decreases, and achieve stable  $T_V^B$  values. However, over the highest  
344 elevations (>2500 m a.s.l.) of the percolation facies approaching the dry snow line, where seasonal surface  
345 melting and the formation of embedded ice structures is limited,  $T_{V,min}^B$  values remain radiometrically warm  
346 during the freezing season.  $T_V^B$  decreases, often step-responses exceeding 10 K, are a result of an increase  
347 in volume scattering from newly formed embedded ice structures within a spatially coherent melt layer.  
348 Temporal L-band signatures that increase several K on time scales of years indicate the burial of spatially  
349 coherent melt layers formed following the 2010, 2012, 2015, and 2018 melting seasons by snow  
350 accumulation.

351 Exponentially decreasing temporal L-band signatures transition smoothly between perennial firn  
352 aquifer, ice slab, and other percolation facies areas – there are no distinct temporal L-band signatures that  
353 delineate boundaries between these sub-facies. Boundary transitions between the dry snow facies and the  
354 wet snow facies, however, are delineated above and below the percolation facies. Over the dry snow facies  
355 (e.g., Fig. 4d, SMAP Test Site D: 66.3649°N, 43.2115°W, 2497 m a.s.l.),  $T_{V,max}^B$  and  $T_{V,min}^B$  values are  
356 radiometrically warm during the melting and freezing seasons. Temporal L-band signatures that increase  
357 on time scales of years are observed throughout the dry snow facies at elevations as high as Summit  
358 Station (3200 m a.s.l.) and indicate the burial of the spatially coherent melt layer formed following the 2012  
359 melting season (Nghiem et al., 2012) by snow accumulation (Culberg et al., 2021). Over the wet snow  
360 facies (e.g., Fig. 4e, SMAP Test Site E: 67.3454°N, 48.4789°W, 1469 m a.s.l.), where seasonal meltwater  
361 is fully refrozen and stored as superimposed ice,  $T_{V,max}^B$  values are radiometrically warm during the melting  
362 season. As compared to the percolation facies, where temporal L-band signatures exhibit rapid increases  
363 following melt onset, temporal L-band signatures reverse and exhibit rapid decreases. These reversals are  
364 a result of high reflectivity and attenuation at the fully water-saturated snow layer and/or at the wet rough  
365 superimposed ice-air interface. Meltwater runs-off superimposed ice downslope towards the ablation facies.  
366  $T_{V,min}^B$  values remain radiometrically warm during the freezing season. Temporal L-band signatures exhibit  
367 rapid increases, and achieve stable  $T_V^B$  values.

### 368 **2.3.2 Two-Layer-L-band Brightness Temperature Model**

369 Based on our analysis of  $T_{V,max}^B$  and  $T_{V,min}^B$  in temporal L-band signatures over the percolation facies  
 370 (Section 2.3.1), we derive a ‘firm saturation’ parameter using a simple two-layer L-band brightness  
 371 temperature model (Ashcraft and Long, 2006; Miller et al., 2021, in press). The ‘firm saturation’ parameter  
 372 is similar to the ‘melt intensity’ parameter derived in Hicks and Long (2011) that uses enhanced resolution  
 373 vertically-polarized Ku-band radar backscatter imagery (2003) collected by the SeaWinds radar  
 374 scatterometer that was flown in tandem on NASA’s Quick SCATterometer (QuikSCAT) satellite (Tsai et al.,  
 375 2000) and JAXA’s Advanced Earth Observing Satellite 2 (ADEOS-II) (Freilich et al., 1994). We use the firm  
 376 saturation parameter to estimate the maximum seasonal volumetric fraction of meltwater within the  
 377 saturated upper snow and firm layers of the percolation facies using  $T_{V,max}^B$  and  $T_{V,min}^B$  values extracted from  
 378  $T_V^B$  time series. We calculate the firm saturation parameter for each rSIR grid cell within the ice sheet-masked  
 379 extent of the GrIS as part of our adapted empirical algorithm (Section 2.3.4).

380 We assume a base layer underlying a water-saturated firm layer with a given depth and volumetric  
 381 fraction of meltwater. Each of the layers is homogenous. The ice sheet is discretely layered to calculate  $T_V^B$   
 382 at an oblique incidence angle (Eq. 1). Emission from the base layer is a function of both the macroscopic  
 383 roughness and the dielectric properties of the layer. It occurs in conjunction with volume scattering at depth,  
 384 and is locally dependent on embedded ice structures, spatially coherent melt layers, ice slabs, and  
 385 perennial firm aquifers. Reflectivity at depth (i.e., at the base layer-water-saturated firm layer interface), and  
 386 at the ice sheet surface (i.e., at the water-saturated firm layer-air interface) is neglected. The contribution  
 387 from each layer is individually calculated.

388 The two-layer L-band brightness temperature model is represented analytically by

$$389 T_{V,max}^B = T(1 - e^{-\kappa_e d \sec \theta}) + T_{V,min}^B e^{-\kappa_e d \sec \theta}, \quad (\text{Eq. 1})$$

390 where  $T_{V,max}^B$  is the maximum vertically-polarized L-band brightness temperature at the ice sheet surface,  
 391 and represents emission from the maximum seasonal volumetric fraction of meltwater stored within the  
 392 water-saturated firm layer.  $T_{V,min}^B$  is the minimum vertically-polarized L-band brightness temperature  
 393 emitted from the base layer.  $T$  is the physical temperature of the water-saturated firm layer,  $\theta$  is the  
 394 transmission angle,  $\kappa_e$  is the extinction coefficient, and  $d$  is depth.

395 We invert Eq. 1 and solve for the firm saturation parameter ( $\xi$ )

$$396 \xi = \ln \left( \frac{T_{V,max}^B - T}{T_{V,min}^B - T} \right) \cos \theta, \quad (\text{Eq. 2})$$

397 where  $\xi = \kappa_e d$ . The maximum vertically-polarized L-band brightness temperature asymptotically approaches  
 398 the physical temperature of the water-saturated firm layer as the extinction coefficient and the depth of the  
 399 water-saturated firm layer increases. For simplicity, we follow Jezek et al., (2015) and define the extinction  
 400 coefficient as the sum of the Raleigh scattering coefficient ( $\kappa_s$ ) and the absorption coefficient ( $\kappa_a$ ). This  
 401 assumes scattering from snow grains, which are small (millimeter scale) relative to the L-band wavelength  
 402 (21 cm), and neglects Mie scattering from large (centimeter scale) embedded ice structures. However, for

403 water-saturated firn, absorption dominates over scattering, and increases in the extinction coefficient are  
 404 controlled by the volumetric fraction of meltwater ( $m_v$ ).

405 We assume that thicker water-saturated firn layers with larger volumetric fractions of meltwater  
 406 generate higher firn saturation parameter values. However, the thickness of the water-saturated firn layer  
 407 is limited by the L-band penetration depth. Theoretical L-band penetration depths calculated for a water-  
 408 saturated firn layer range from between 10 m for small volumetric fractions of meltwater ( $m_v < 1\%$ ), and 1  
 409 cm for large volumetric fractions of meltwater ( $m_v = 20\%$ ) (Fig. 5). Large volumetric fractions of meltwater  
 410 results in high reflectivity and attenuation at the water-saturated firn layer-air interface-, and a radiometrically  
 411 cold firn layer.

### 412 **2.3.3 Continuous Logistic Model**

413 We adapt our previously developed empirical algorithm to map the extent of Greenland's perennial firn  
 414 aquifers (Miller et al., 2020) to also map the extent of ice slab areas. The empirical algorithm is derived from  
 415 the continuous logistic model, which is based on a differential equation that models the decrease in physical  
 416 systems as a function of time using a set of sigmoidal curves. These curves begin at a maximum value with  
 417 an initial interval of decrease that is approximately exponential. Then, as the function approaches its  
 418 minimum value, the decrease slows to approximately linear. Finally, as the function asymptotically reaches  
 419 its minimum value, the decrease exponentially tails off and achieves stable values. We use the continuous  
 420 logistic model to parametrize the refreezing rate within the water-saturated upper snow and firn layers of  
 421 the percolation facies using  $T_V^B$  time series that are partitioned using  $T_{V,max}^B$  and  $T_{V,min}^B$  values. We calculate  
 422 the refreezing rate for each rSIR grid cell within the percolation facies extent as part of our adapted empirical  
 423 algorithm (Section 2.3.4).

424 The continuous logistic model is described by a differential equation known as the logistic equation

$$425 \quad \frac{dx}{dt} = \zeta x(1 - x) \quad (\text{Eq. 3})$$

426 that has the solution

$$427 \quad x(t) = \frac{1}{1 + \left(\frac{1}{x_0} - 1\right)e^{-\zeta t}}, \quad (\text{Eq. 4})$$

428 where  $x_0$  is the function's initial value,  $\zeta$  is the function's exponential rate of decrease, and  $t$  is time. The  
 429 function  $x(t)$  is also known as the sigmoid function. We use the sigmoid function to model the exponentially  
 430 decreasing temporal L-band signatures observed over the percolation facies as a set of decreasing  
 431 sigmoidal curves.

432 We first normalize  $T_V^B$  time series for each rSIR grid cell

$$433 \quad T_{V,N}^B(t) = \frac{T_V^B(t) - T_{V,min}^B}{T_{V,max}^B - T_{V,min}^B}, \quad (\text{Eq. 5})$$

434 where  $T_{V,min}^B$  is the minimum vertically-polarized L-band brightness temperature, and  $T_{V,max}^B$  is the maximum  
 435 vertically-polarized L-band brightness temperature. We then apply the sigmoid fit

436 
$$T_{V,N}^B(t \in [t_{max}, t_{min}]) = \frac{1}{1 + \left( \frac{1}{T_{V,N}^B(t_{max})} - 1 \right) e^{-\zeta t}} . \quad (\text{Eq. 6})$$

437  $T_{V,N}^B(t \in [t_{max}, t_{min}])$  is the normalized vertically-polarized L-band brightness temperature on the time  
 438 interval  $t \in [t_{max}, t_{min}]$ , where  $t_{max}$  is the time the function achieves a maximum value, and  $t_{min}$  is the  
 439 time the function achieves a minimum value. The initial normalized vertically-polarized L-band brightness  
 440 temperature ( $T_{V,N}^B(t_{max})$ ) is the function's maximum value. The final normalized vertically-polarized L-band  
 441 brightness temperature ( $T_{V,N}^B(t_{min})$ ) is the function's minimum value. The function's exponential rate of  
 442 decrease represents the refreezing rate parameter ( $\zeta$ ). An example set of simulated sigmoidal curves is  
 443 shown in Fig. 6.

#### 444 **2.3.4 SMAP-Derived Perennial Firn Aquifer and Ice Slab Mapping**

445 Our adapted empirical algorithm is implemented in two steps: (1) mapping the extent of the percolation  
 446 facies using the firn saturation parameter derived from the simple two-layer L-band brightness temperature  
 447 model (Section 2.3.2), and (2) mapping the extent of perennial firn aquifer and ice slab areas over the  
 448 percolation facies using the continuous logistic model (Section 2.3.3) we calibrate using airborne ice-  
 449 penetrating radar surveys (Section 2.2).

450 Using Eq. 2, we first set a threshold for the firn saturation parameter ( $\xi_T$ ) defined by the relationship

451 
$$\xi_T = (\kappa_s + \kappa_a)d \leq \xi . \quad (\text{Eq. 7})$$

452 We calculate the Raleigh scattering coefficient ( $\kappa_s$ ) in Eq. 7 using

453 
$$\kappa_s = N_d \frac{8}{3} k_o^4 r^6 \left| \frac{\epsilon_r - 1}{\epsilon_r + 2} \right|^2 , \quad (\text{Eq. 8})$$

454 where  $N_d$  is the particle density,  $k_o$  is the wave number of the background medium of air,  $r$  is the snow  
 455 grain radius set to  $r=2$  mm, and  $\epsilon_r$  is the complex dielectric constant. The particle density is defined by

456 
$$N_d = \frac{\rho_{firn}}{\rho_{ice}} \frac{1}{\frac{4}{3}\pi r^3} , \quad (\text{Eq. 9})$$

457 where  $\rho_{firn}$  is firn density set to  $\rho_{firn}=400$  kg/m<sup>3</sup>, and  $\rho_{ice}$  is ice density set to  $\rho_{ice}=917$  kg/m<sup>3</sup>. Our grain  
 458 radius and firn density estimates are consistent with measurements within the upper snow and firn layers  
 459 of the percolation facies of south eastern Greenland at the Helheim Glacier field site (Fig. 2a, blue circle),  
 460 where in situ perennial firn aquifer measurements have recently been collected (Miller et al., 2017).

461 We calculate the absorption coefficient ( $\kappa_a$ ) in Eq. 7 using

462 
$$\kappa_a = -2k_o \Im\{\sqrt{\epsilon_r}\} , \quad (\text{Eq. 10})$$

463 where  $\Im\{\}$  represents the imaginary part. We calculate the complex dielectric constant of the water-  
 464 saturated firn layer in Eq. 8 and Eq. 10 using the empirically derived models described in Tiuri et al., (1984).  
 465 We set the volumetric fraction of meltwater to  $m_v=1\%$ . We set the depth of the water-saturated firn layer in  
 466 Eq. 7 to  $d=1$  m. These values are consistent with typical lower frequency (e.g., 37 GHz, 13.4 GHz, 19 GHz)  
 467 passive (e.g., Mote, et al. 1995; Abdalati and Steffen, 1997; Ashcraft and Long, 2006) and active (e.g.,

468 Hicks and Long, 2011) microwave algorithms used to detect seasonal surface melting over the GrIS. Using  
469 the results of Eq. 7, 8, 9, and 10, we calculate the firn saturation parameter threshold to be  $\xi_T=0.1$ .

470 The first step in our adapted empirical algorithm is to map the extent of the percolation facies. For  
471 each rSIR grid cell within the ice ~~sheet~~-masked extent of the GrIS, we smooth the corresponding  $T_V^B$  time  
472 series using a 14-observation (1 week) moving window. We extract the minimum vertically-polarized L-  
473 band brightness temperature ( $T_{V,min}^B$ ), and the maximum vertically-polarized L-band brightness temperature  
474 ( $T_{V,max}^B$ ). We set the physical temperature of the water-saturated firn layer to  $T=273.15$  K, and the  
475 transmission angle to  $\theta=40^\circ$ . We then calculate the firn saturation parameter ( $\xi$ ) using Eq. 2. If the  
476 calculated firn saturation parameter exceeds the firn saturation parameter threshold, the rSIR grid cell is  
477 converted to a binary parameter to map the total extent of the percolation facies.

478 We note that smoothing  $T_V^B$  time series will mask brief low-intensity seasonal surface melting that  
479 occurs in the high-elevation (>2500 m) percolation facies, where seasonal meltwater is rapidly refrozen  
480 within the colder snow and firn layers (e.g., Fig. 4d). Thus, the calculated firn saturated parameter will not  
481 exceed the firn saturation parameter threshold, and these rSIR grid cells are excluded from the algorithm.  
482 The exclusion of rSIR grid cells in the high-elevation percolation facies is not expected to have a significant  
483 impact on our results as our algorithm targets rSIR grid cells in areas that experience intense seasonal  
484 surface melting. The exclusion of rSIR grid cells may slightly underestimate the mapped percolation facies  
485 extent.

486 The second step in our adapted empirical algorithm is to map the extent of perennial firn aquifer  
487 and ice slab areas over the percolation facies. For each rSIR grid cell within the mapped percolation facies  
488 extent, we normalize the corresponding  $T_V^B$  time series ( $T_{V,N}^B(t)$ ) using Eq. 5. We then extract the initial  
489 normalized vertically-polarized L-band brightness temperature ( $T_{V,N}^B(t_{max})$ ) and the final normalized  
490 vertically-polarized L-band brightness temperature ( $T_{V,N}^B(t_{min})$ ), and partition  $T_{V,N}^B(t)$  on the time interval  $t \in$   
491  $[t_{max}, t_{min}]$ . We smooth  $T_{V,N}^B(t \in [t_{max}, t_{min}])$  using a 56-observation (4 week) moving window. The  
492 sigmoid fit is then iteratively applied using Eq. 6. Smoothing reduces the chi-squared error statistic when  
493 fitting  $T_{V,N}^B(t \in [t_{max}, t_{min}])$  to the sigmoid function. We fix the initial normalized vertically-polarized L-band  
494 brightness temperature at  $T_{V,N}^B(t_{max})=0.99$ , which provides a uniform parameter space in which the  
495 refreezing rate parameter ( $\zeta$ ) can be analyzed. Variability in  $T_{V,N}^B(t_{max})$  is controlled by the volumetric  
496 fraction of meltwater within the upper snow and firn layers of the percolation facies, and is accounted for in  
497 the firn saturation parameter ( $\xi$ ), which is analyzed separately.  $T_{V,N}^B(t \in [t_{max}, t_{min}])$  iteratively fit to the  
498 sigmoid function converge quickly (i.e., algorithm iterations  $I \in [5, 15]$ ), and observations are a good fit (i.e.,  
499 chi squared error statistic is  $\chi^2 \in [0, 0.1]$ ).

500 Using the SMAP-derived  $T_{V,N}^B(t_{max})$  and  $T_{V,N}^B(t_{min})$ , rather than the MODIS-derived initial  
501 normalized vertically-polarized L-band brightness temperature at the surface freeze-up date ( $T_{V,N}^B(t_{sfu})$ ),  
502 and final normalized vertically-polarized L-band brightness temperature at the melt onset date ( $T_{V,N}^B(t_{mo})$ )  
503 that were used in the empirical algorithm described in Miller et al., 2020 has several advantages. They key

504 advantage of this approach is that maps can be generated using  $T^B$  imagery collected from a single satellite,  
505 which simplifies our adapted empirical algorithm. Another advantage is that unlike  $T^B$  collected at shorter-  
506 wavelength thermal infrared frequencies (e.g., MODIS),  $T^B$  collected at longer wavelength microwave  
507 frequencies (e.g., SMAP) is not sensitive to clouds, which eliminates observational gaps and cloud  
508 contamination, and provides more accurate time series partitioning and more robust curve fitting.

509 We calibrate our adapted empirical algorithm using the AR- and MCoRDS-derived perennial firn  
510 aquifer and ice slab detections projected on the NH EASE-Grid 2.0. For each rSIR grid cell with at least  
511 one detection, we extract the correlated maximum vertically-polarized L-band brightness temperature  
512 ( $T_{V,max}^B$ ), the minimum vertically-polarized L-band brightness temperature ( $T_{V,min}^B$ ), the firn saturation  
513 parameter ( $\xi$ ), and the refreezing rate parameter ( $\zeta$ ). For each of the extracted calibration parameters, we  
514 calculate the standard deviation ( $\sigma$ ). Thresholds of  $\pm 2\sigma$  are set in an attempt to eliminate peripheral rSIR  
515 grid cells near the ice sheet edge and near the boundaries of each sub-facie, where L-band emission can  
516 be influenced by morphological features, such as crevasses, superimposed and glacial ice, and spatially  
517 integrated with emission from rock, land, the ocean, and adjacent percolation facies and wet snow facies  
518 areas. The calibration parameter intervals are given in Table 2. We apply the calibration to each rSIR grid  
519 cell within the percolation facies extent. If the extracted calibration parameters are within the intervals, the  
520 rSIR grid cell is converted to a binary parameter to map the total extent of each of these sub-facies.

521 Miller et al., 2020 cited significant uncertainty in the SMAP-derived perennial firn aquifer extent as  
522 a result of the lack of a distinct temporal L-band signature delineating the boundary between perennial firn  
523 aquifer areas and adjacent percolation facies areas. In this study, similar uncertainty exists in the SMAP-  
524 derived perennial firn aquifer and ice slab extents. This uncertainty could, at least in part, be a result of the  
525 rSIR algorithm. An rSIR grid cell corresponds to the weighted average of  $T^B$  over SMAP's antenna footprint  
526 (Long et al., 2020). The weighting is the grid cell's spatial response function (SRF), which is approximately  
527 18 km (i.e., the effective resolution) in diameter. The SRF is centered on the rSIR grid cell. Since the  
528 effective resolution (i.e., the size of the 3 dB contour of the SRF) is less than the rSIR grid cell spacing,  
529 rSIR grid cell SRF's overlap and the grid cells  $T^B$  values are not statistically independent. This uncertainty,  
530 however, could also have a geophysical basis, as it is unlikely that the boundaries between sub-facies as  
531 well as between facies are distinct. The thickness of the water-saturated firn layer or ice slab may thin and  
532 taper-off at the periphery, and sub-facies and facies may become spatially scattered and merge together.

533 The limited extent (AR, 15 m x 20 m; MCoRDS, 14 m x 40 m) of the airborne ice-penetrating radar  
534 surveys as compared to the rSIR grid cell extent (3.125 km) and the effective resolution of the SMAP  
535 enhanced-resolution  $T_V^B$  imagery is also cited in Miller et al., 2020 as a source of uncertainty in the empirical  
536 algorithm. In this study, similar uncertainty exists in our adapted empirical algorithm. The total rSIR grid cell  
537 extent with airborne ice-penetrating radar survey coverage is less than 2%. Thus, 98% of the total rSIR grid  
538 cell extent from which the SMAP-derived calibration parameter intervals are extracted is unknown.  
539 Calculating the total rSIR grid cell extent where detections are absent along OIB flight lines and statistically  
540 integrating this calculation into the multi-year calibration technique may help reduce the uncertainty,

541 particularly the significant uncertainty in the interannual variability in extent, which we have yet to resolve.  
542 A sensitivity analysis suggests that even small changes in the SMAP-derived calibration parameter intervals  
543 (i.e., several K for  $T_{V,min}^B$ , and  $T_{V,max}^B$ , several tenths of a percentage point for  $\xi$ , and several hundredths of  
544 a percentage point for  $\zeta$ ) can result in variability in the mapped extents of hundreds of square kilometers,  
545 and boundary transitions between perennial firn aquifer and ice slab areas. Thus, the mapped extent of  
546 each of these sub-facies should simply be considered an initial result demonstrating the potential of our  
547 adapted empirical algorithm for future work.

### 548 **3. Results and Discussion**

549 The SMAP-derived maximum vertically-polarized L-band brightness temperature values generated by our  
550 adapted empirical algorithm range from between  $T_{V,max}^B=150$  K and 275 K, and the minimum vertically-  
551 polarized L-band brightness temperature values range from between  $T_{V,min}^B=130$  K and 250 K. These values  
552 are consistent with the range of  $T_{V,max}^B$  and  $T_{V,min}^B$  values given in the temporal L-band signature analysis  
553 (Table 1). Firn saturation parameter values range from between  $\xi=0.1$  and 4.0. Refreezing rate parameter  
554 values range from between  $\zeta=-0.09$  and -0.01. The observed lower bound ( $\zeta=-0.09$ ) of the refreezing rate  
555 parameter is significantly higher than the predicted lower bound ( $\zeta=-1$ ) in our example set of simulated  
556 sigmoidal curves (black line, Fig. 6).

557 The SMAP-derived perennial firn aquifer, ice slab, and percolation facies extents are shown in Figs.  
558 7a-9a. The percolation facies extent ( $5.8 \times 10^5$  km<sup>2</sup>) is mapped at elevations between 500 m a.s.l. and  
559 3000 m a.s.l., and extends over 32 % of the GrIS extent ( $1.8 \times 10^6$  km<sup>2</sup>). The perennial firn aquifer extent  
560 (64,000 km<sup>2</sup>) is mapped at elevations between 600 m a.s.l and 2600 m a.s.l., and extends over 11% of the  
561 percolation facies extent, and 4% of the GrIS extent. Predominately high  $T_{V,max}^B$ ,  $T_{V,min}^B$ ,  $\xi$ , and  $\zeta$  values  
562 mapped within the perennial firn aquifer extent indicates the widespread presence of thicker water-  
563 saturated firn layers with larger volumetric fractions of meltwater that are radiometrically warm during both  
564 the melting and freezing seasons, and have extended refreezing rates. The ice slab extent (76,000 km<sup>2</sup>) is  
565 mapped at elevations between 800 m a.s.l and 2700 m a.s.l., and extends over 13 % of the percolation  
566 facies extent, and 4 % of the GrIS extent. As compared to perennial firn aquifer areas, decreased  $T_{V,max}^B$ ,  
567  $T_{V,min}^B$ ,  $\xi$  and  $\zeta$  values in ice slabs areas indicates the presence of thinner water-saturated firn layers with  
568 lower volumetric fractions of meltwater that are radiometrically colder, and have slightly more rapid  
569 refreezing rates. Combined together, the total extent (140,000 km<sup>2</sup>) is the equivalent of 24% of the  
570 percolation facies extent, and 10% of the GrIS extent. The extents of these sub-facies are generally isolated  
571 and somewhat scattered within the percolation facies. However, in several areas in south, south and central  
572 eastern, and northern Greenland, the sequential formation of facies and sub-facies (dry snow facies -  
573 percolation facies - ice slab - perennial firn aquifer – ablation facies) is are mapped.

574 Figs. 7b-9b shows perennial firn aquifers, ice slabs, and spatially coherent melt layers detected by  
575 airborne ice-penetrating radar surveys overlaid on the SMAP-derived percolation facies extent. The SMAP-



576 derived perennial firn aquifer extent mapped in southern, and south and central eastern Greenland is  
577 consistent with the AR- and MCoRDS-derived perennial firn aquifer detections. Additional smaller perennial  
578 firn aquifer areas are mapped in northern Greenland. The SMAP-derived ice slab extent mapped in south  
579 western, and central eastern Greenland is generally consistent with the spatial patterns of the AR-derived  
580 ice slab detections, however, is significantly expanded upslope in each of these areas. In northern  
581 Greenland, perennial firn aquifers areas are alternatively mapped, and additional expansive ice slab areas  
582 are mapped upslope of perennial firn aquifer areas. Additional smaller ice slab areas are mapped in south  
583 and south eastern Greenland. We note that the AR- and MCoRDS-derived perennial firn aquifer and ice  
584 slab detections are limited in space and time, particularly in northern Greenland, with a time interval as  
585 large as nine years between the airborne ice-penetrating radar surveys and the SMAP enhanced-resolution  
586  $T_V^B$  imagery we use in our adapted empirical algorithm. In western and northern Greenland, the 2015 melting  
587 season was especially intense (Tedesco et al., 2016). And, in northern Greenland, the ablation facies have  
588 recently (2010-2019) increased in extent (Noël et al., 2019), and supraglacial lakes have recently (2014-  
589 2019) advanced inland (Turton et al., 2021), indicating a possible geophysical basis for the observed  
590 formation, boundary transitions, and expansion. Neither perennial firn aquifer or ice slab areas are mapped  
591 on the Maniitsoq and Flade Isblink Ice Caps, where spatially integrated L-band emission results in  
592 calibration parameter values outside the defined intervals for each of these sub-facies.

593 Although the AR-derived spatially coherent melt layers detections are often observed to be adjacent  
594 to perennial firn aquifer and ice slab areas, these sub-facies were masked in the original airborne ice  
595 penetrating radar survey analysis by Culberg et al., (2021). Spatially coherent melt layers often overlay  
596 perennial firn aquifers (e.g., Fig. 3a), and merge with ice slabs (Culberg et al., 2021; Fig.4).

597 Shallow buried supraglacial lakes have recently been identified within the percolation facies of  
598 western, northern, and north and central eastern Greenland using airborne ice-penetrating radar surveys  
599 (Koenig et al., 2015) and satellite synthetic aperture radar imagery (Miles et al., 2017; Schröder et al., 2020;  
600 Dunmire et al., 2021). These buried supraglacial lakes are within the SMAP-derived perennial firn aquifer  
601 and ice slab extents, however, are not expected to significantly influence L-band emission in these areas  
602 for two reasons. (1) As compared to SMAP's 18 km footprint, the mean extent of buried supraglacial lakes  
603 is limited (less than 1 km<sup>2</sup>), and they are sparsely distributed in perennial firn aquifer and ice slab areas  
604 (Dunmire et al., 2021). (2) Supraglacial lakes form during the melting season as a result of meltwater  
605 storage within topographic depressions at the ice sheet surface (Echelmeyer et al. 1991). Similar to  
606 subglacial lakes (Jezek et al., 2015) and perennial firn aquifers (Miller et al., 2020), supraglacial lakes  
607 represent radiometrically cold near-surface meltwater reservoirs. Upwelling L-band emission from deeper  
608 firn layers, superimposed and/or glacial ice, and the underlying bedrock are effectively blocked by high  
609 reflectivity and attenuation at the interface between the lake bottom and the underlying impermeable layer.  
610 This results in low observed  $T^B$  at the upper surface of meltwater stored within supraglacial lakes. During  
611 the freezing season, the upper surface of meltwater refreezes and forms a partial or solid-ice cap that is  
612 sometimes buried by snow accumulation (Koenig et al., 2015). Airborne ice-penetrating radar surveys in

613 April and May between 2009 and 2012 suggest the mean depth to the upper surface of meltwater stored  
614 within buried supraglacial lakes is approximately 2 m (Koenig et al., 2015). Over buried supraglacial lakes,  
615 L-band emission from the refreezing partial or solid-ice cap, which is smooth relative to the L-band  
616 wavelength (21 cm), likely induces surface scattering. As a result,  $T_V^P$  decreases over buried supraglacial  
617 lakes are likely negligible. Thus, over SMAP's 18 km footprint, we postulate water-saturated firn layers  
618 dominate L-band emission over the percolation facies of the GrIS.

619 The SMAP-derived perennial firn aquifer extent (64,000 km<sup>2</sup>) generated by our adapted empirical  
620 algorithm and the multi-year calibration technique (2015-2019) is consistent with the extent (66,000 km<sup>2</sup>)  
621 generated by the previously developed empirical algorithm and the single-coincident year calibration  
622 technique (2016) described in Miller et al., 2020. The SMAP-derived perennial firn aquifer extent is generally  
623 consistent with previous C-band (5.3 GHz) satellite radar scatterometer-derived perennial firn aquifer  
624 extents mapped using the Advanced SCATterometer (ASCAT) on the European Organization for the  
625 Exploitation of Meteorological Satellites (EUMETSAT) Meteorological Operational A (MetOp-A) satellite  
626 (2009-2016, 52 000-153 000 km<sup>2</sup>; Miller, 2019), and the Active Microwave Instrument in radar scatterometer  
627 mode (ESCAT) on ESA's European Remote Sensing (ERS) satellite series (1992-2001, 37 000-64 000 km<sup>2</sup>;  
628 Miller, 2019) as well as the C-band (5.4 GHz) synthetic aperture radar-derived extent mapped using ESA's  
629 Sentinel-1 satellite (2014-2019, 54 000 km<sup>2</sup>; Brangers et al., 2020). The exception is the ASCAT-derived  
630 perennial firn aquifer extent (2012-2013, 153,000 km<sup>2</sup>; Miller, 2019) mapped following the 2012 melting  
631 season (Nghiem et al., 2012) in which significant changes in the dielectric and geophysical properties that  
632 influence radar backscatter likely occurred. The unreasonably expansive (i.e., more than twice the mean)  
633 mapped extent is a result of ASCAT'S shallow (several meters) C-band penetration depth (Jezek et al.,  
634 1994), and the simple threshold-based algorithm, which was not calibrated for an extreme melting season  
635 that included saturation of the upper snow and firn layers of the dry snow facies and percolation facies with  
636 relatively large volumetric fractions of meltwater (Miller et al., 2019). Water-saturated firn layers had  
637 extended refreezing rates, however, seasonal meltwater was not stored at depth. Widespread spatially  
638 coherent melt layers were alternatively formed in many of the mapped areas (Culberg et al., 2021). The  
639 SMAP-derived ice slab extent (76,000 km<sup>2</sup>) is also consistent with previous AR-derived ice slab extents  
640 (2010-2014, 64,800 km<sup>2</sup>-69,400 km<sup>2</sup>; MacFerrin et al., 2019).

641 Although we simply consider our mapped extents a high-probability area for preferential formation,  
642 the maps generated by our adapted empirical algorithm and the multi-year calibration technique for  
643 individual years suggest there reasonable interannual variability in perennial firn aquifer and ice and slab  
644 extents (Table 3). Our results demonstrate sensitivity to the variability in the depth- and time-integrated  
645 dielectric and geophysical properties of the percolation facies that influence the radiometric temperature,  
646 even during the 2015 melting season (Tedesco et al., 2016).

#### 647 **4 Implications**

648 Seasonal surface melting over the GrIS has increased in extent, intensity, and duration since early in the  
649 satellite era (Steffen et al., 2004; Tedesco e al., 2008; Tedesco et al., 2011; Nghiem et al., 2012; Tedesco

650 et al., 2016; Tedesco and Fettweis, 2020; Cullather et al., 2020). Consistent with recent seasonal surface  
651 melting trends, meltwater runoff has accelerated to become the dominant mass loss mechanism over the  
652 GrIS (van den Broeke et al., 2016). Meltwater storage in both solid (i.e., embedded ice structures, including  
653 ice slabs, and spatially coherent melt layers) and liquid (i.e., perennial firn aquifers) form can buffer  
654 meltwater runoff in the percolation facies and delay its eventual release into the ocean (Harper et al., 2012).  
655 However, significant uncertainty remains in meltwater runoff estimates as a result of the lack of knowledge  
656 of heterogeneous infiltration and refreezing processes within the snow and firn layers (Pfeffer and  
657 Humphrey, 1996), and the depths to which meltwater can descend beneath the ice sheet surface  
658 (Humphrey et al., 2012).

659         If the increasing seasonal surface melting trend continues (Franco et al., 2013; Noël et al., 2021),  
660 perennial firn aquifer formation and expansion may increase the possibility of crevasse-deepening via  
661 meltwater-induced hydrofracturing (Alley et al., 2005; van der Veen, 2007), especially if crevasse fields  
662 expand into perennial firn aquifer areas as a result of accelerated ice flow (Colgan et al., 2016). Meltwater-  
663 induced hydrofracturing is an important component of supraglacial lake drainage during the melting season  
664 (Das et al., 2008; Stevens et al., 2015) leading to at least temporary localized accelerated ice flow velocities  
665 (Zwally et al., 2002; Joughin et al., 2013; Moon et al., 2014) as well as ice discharge from outlet glaciers  
666 (Chudley et al., 2019), and mass balance changes (Joughin et al., 2008). Perennial firn aquifers may also  
667 support meltwater-induced hydrofracturing, even during the freezing season (Poinar et al., 2017; Poinar et  
668 al., 2019).

669         The formation and expansion of ice slabs reduces permeability within the upper snow and firn  
670 layers and facilitates lateral meltwater flow with minimum vertical percolation into the deeper firn layers,  
671 thereby enhancing meltwater runoff and mass loss at the periphery ([Machguth et al., 2016](#); [MacFerrin et](#)  
672 [al., 2019](#)). Lateral meltwater flow across ice layers overlying deeper permeable firn layers was first  
673 postulated by Müller (1962). The theory was then further developed by Pfeffer et al., (1991) as an end-  
674 member case for meltwater runoff in the percolation facies, with the other end member case being lateral  
675 meltwater flow across superimposed ice. Lateral meltwater flow and high-elevation (1850 m a.s.l) meltwater  
676 runoff across ice slabs in the percolation facies was ~~recently~~ first observed in visible satellite imagery  
677 collected by the NASA-USGS Landsat 7 mission during the 2012 melting season ([Machguth et al., 2016](#)).

678         Spatially coherent melt layers represent a ~~newly~~ recently identified refreezing mechanism in the  
679 dry snow facies ([Nghiem et al., 2002](#); Culberg et al., 2021). Similar to ice slabs, the formation and expansion  
680 of spatially coherent melt layers reduces the pore space within the upper snow and firn layers, and can limit  
681 meltwater flow with minimum vertical percolation into the deeper firn layers, thereby potentially  
682 preconditioning the dry snow facies for the formation of ice slabs and enhanced meltwater runoff from  
683 significantly higher elevations on accelerated time scales. If spatially coherent melt layers merge with ice  
684 slabs upslope of perennial firn aquifers areas they might also simultaneously accelerate both meltwater  
685 runoff and meltwater-induced hydrofracturing during extreme melting seasons. The formation of spatially  
686 coherent melt layers overlying deeper perennial firn aquifers may result in the formation of shallow perched

687 firn aquifers (Culberg et al., 2021;—), or may terminate gravity-driven meltwater drainage and seasonal  
688 recharging (Fountain and Walder, 1998), which may eventually completely refreeze stored meltwater into  
689 ice slabs or decameters thick solid-ice layers overlying deeper glacial ice.

## 690 **5 Summary and Future Work**

691 In this study, for the first time, we have demonstrated the novel use of the L-band microwave radiometer  
692 on NASA's SMAP satellite for mapping perennial firn aquifers and ice slabs together as a continuous system  
693 over the percolation facies of the GrIS. We have adapted our previously developed empirical algorithm  
694 (Miller et al., 2020) by expanding our analysis of spatiotemporal differences in SMAP enhanced-resolution  
695  $T_V^B$  imagery and temporal L-band signatures. We have used this analysis to derive a firn saturation  
696 parameter from a simple two-layer L-band brightness temperature model (Miller et al., 2021). And, we have  
697 used the firn saturation parameter to map the extent of the percolation facies. We have found that by  
698 correlating maximum and minimum  $T_V^B$  values, the firn saturation parameter, and the refreezing rate  
699 parameter with perennial firn aquifer and ice slab detections identified via the CReSIS AR and MCoRDS  
700 instruments flown by NASA's OIB campaigns that we can calibrate our previously developed empirical  
701 algorithm (Miller et al., 2020) to map plausible extents.

702 We note that significant uncertainty exists in the mapped extents as a result of: (1) correlating the  
703 SMAP-derived parameters with airborne ice-penetrating radar detections that are not coincident in time, (2)  
704 the lack of a distinct temporal L-band signature delineating the boundary between perennial firn aquifer  
705 areas, ice slabs areas, and adjacent percolation facies areas, and (3) the limited extent of the airborne ice-  
706 penetrating radar detections as compared to the rSIR grid cell extent and the effective resolution of the  
707 SMAP enhanced-resolution  $T_V^B$  imagery.

708 Miller et al., (2020) normalized SMAP enhanced-resolution  $T_V^B$  time series and converted the  
709 exponential rate of  $T_V^B$  decrease over perennial firn aquifer areas to a binary parameter to map extent. In  
710 this study, we have converted the SMAP-derived parameters to binary parameters to map the extent of  
711 both perennial firn aquifer and ice slab areas. Moreover, we have included additional analysis of the  
712 spatiotemporal differences in maximum and minimum  $T_V^B$  values, the firn saturation parameter, and the  
713 refreezing rate parameter. We have shown that spatiotemporal differences in the SMAP-derived  
714 parameters are consistent with our assumption of spatiotemporal differences in the englacial hydrology and  
715 thermal characteristics of firn layers at depth.

716 Future work will focus on simulating temporal L-band signatures observed over perennial firn  
717 aquifer and ice slab areas for a wide range of geophysical properties. Additionally, we will simulate the  
718 distinct temporal L-band signatures observed over spatially coherent melt layers and explore mapping the  
719 extent. Combining multi-layer depth-integrated L-band brightness temperature models (e.g., Jezek et al.,  
720 2015) that include embedded ice structure parametrizations (e.g., Jezek et al., 2018) with models of depth-  
721 dependent geophysical parameters can lead to an improved understanding of the extremely complex and  
722 poorly described physics controlling L-band emission over the percolation facies. The development of more

723 sophisticated empirical algorithms that incorporate multi-layer depth-integrated L-band brightness  
724 temperature models that are constrained by in situ measurements can help reduce the significant  
725 uncertainty in the current mapped extents, and provide more accurate boundary delineation that can be  
726 used to further quantify the interannual variability in future mapped extents of perennial firn aquifer, ice slab  
727 and spatially coherent melt layer areas.

## 728 **Data Availability**

729 SMAP Radiometer Twice-Daily rSIR-Enhanced EASE-Grid 2.0 Brightness Temperatures, Version 1 (2015-  
730 2019) have been produced as part of the NASA Science Utilization of SMAP project and are available at  
731 <https://doi.org/10.5067/QZ3WJNOUZLFK> (Brodzik et al., 2019). The NASA MEaSURES Greenland Ice  
732 Mapping Project (GIMP) Land Ice and Ocean Classification Mask, Version 1, is available at  
733 <https://doi.org/10.5067/B8X58MQBFUPA> (Howat, 2017), and the Digital Elevation Model, Version 1, is  
734 available at <https://nsidc.org/data/nsidc-0645/versions/1> (Howat et al., 2015). The coastline data are  
735 available from GSHHG – A Global Self-consistent, Hierarchical, High-resolution Geography Database  
736 <https://doi.org/10.1029/96JB00104> (Wessel and Smith, 1996). Ice surface temperature imagery (2015-  
737 2019) have been produced as part of the Multilayer Greenland Ice Surface Temperature, Surface Albedo,  
738 and Water Vapor from MODIS V001 data set and are available at  
739 <https://doi.org/10.5067/7THUWT9NMPDK> (Hall and DiGirolamo, 2019). OIB AR- and MCoRDS-derived  
740 perennial firn aquifers detections (2010-2017) are available at  
741 <https://arcticdata.io/catalog/view/doi:10.18739/A2985M> (Miège et al., 2016). OIB AR-derived ice slab  
742 detections (2010-2014) are available at <https://doi.org/10.6084/m9.figshare.8309777> (MacFerrin et al.,  
743 2019). OIB AR-derived spatially coherent melt layer detections (2017) are available at  
744 (<https://doi.org/10.18739/A2736M33W>) (Culberg et al., 2021). OIB AR L1B Geolocated Radar Echo  
745 Strength Profiles, Version 2, are available at, <https://doi.org/10.5067/OZY1XYHNIQNY> (Paden et al., 2018).  
746 NASA MEaSURES MODIS Mosaic of Greenland (MOG) 2015 Image Map, Version 2, is available at  
747 <https://nsidc.org/data/NSIDC-0547/versions/2> (Haran et al., 2018). SMAP-derived perennial firn aquifer ~~and~~  
748 ice slab , ~~and~~ ~~perched~~ ~~firn~~ ~~aquifer~~ extents are available at  
749 <https://zenodo.org/record/5745983#.YabDdNDMKUk>. ~~from JZM upon request.~~

## 750 **Author Contributions**

751 JZM initiated the study, adapted the empirical model, performed the analyses, and wrote the manuscript.  
752 RC processed and interpreted the OIB AR radargram profiles. ~~RC and DMS provided the spatially coherent~~  
753 ~~melt layer detections.~~ All authors participated in discussions and reviewed manuscript drafts.

## 754 **Competing Interests**

755 The authors declare that they have no conflict of interest.

## 756 **Financial Support**

757 JZM, DGL, and MJB are supported by the NASA SMAP Science Team (no. 80NSSC20K1806), and by the  
758 NASA Cryospheric Science Program (no. 80NSSC18K1055 and no. 80NSSC21K0749) under grants to the  
759 University of Colorado and Brigham Young University. RC is supported by a National Defense Science and  
760 Engineering Graduate Fellowship. RC and DMS are supported in part by NASA (no. NNX16AJ95G and  
761 NSF (no. 1745137). CAS is supported by the NASA Headquarters Cryospheric Science Program. We  
762 acknowledge the use of data from CReSIS generated with support from the University of Kansas, NASA  
763 Operation IceBridge (no. NNX16AH54G), NSF (no. ACI-1443054, OPP-1739003, IIS-1838230), Lilly  
764 Endowment Incorporated, and Indiana METACyt Initiative.

## 765 **References**

- 766 Abdalati, W., and Steffen, K.: Snowmelt on the Greenland Ice Sheet as derived from passive microwave  
767 satellite data, *J. Climate*, 10, 165-175, [https://doi.org/10.1175/1520-  
768 0442\(1997\)010<0165:SOTGIS>2.0.CO;2](https://doi.org/10.1175/1520-0442(1997)010<0165:SOTGIS>2.0.CO;2), 1997.
- 769
- 770 Alley, R. B., Dupont, T. K., Parizek, B. R., Anandakrishnan, S.: Access of surface meltwater to beds of sub-  
771 freezing glaciers: Preliminary insights, *Ann. Glaciol.*, 40, 8-14,  
772 <https://doi.org/10.3189/172756405781813483>, 2005.
- 773
- 774 Ashcraft, I. and Long, D.: Comparison of methods for melt detection over Greenland using active and  
775 passive microwave measurements, *Int. J. Remote Sens.*, 27, 2469-2488,  
776 <https://doi.org/10.1080/01431160500534465>, 2006.
- 777
- 778 Benson, C. S.: Stratigraphic studies in the snow and firn of the Greenland Ice Sheet, Ph.D. thesis, California  
779 Institute of Technology, 228 pp., 1960.
- 780
- 781 Brangers, I., Lievens, H., Miège, C., Demuzere, M., Brucker, L., and De Lannoy, G. J. M.: Sentinel-1 detects  
782 firn aquifers in the Greenland Ice Sheet, *Geophys. Res. Lett.*, 47, [e2019GL085192](https://doi.org/10.1029/2019GL085192),  
783 <https://doi.org/10.1029/2019GL085192>, 2020.
- 784
- 785 Brodzik, M. J., Long, D. G., and Hardman, M. A.: SMAP Radiometer Twice-Daily rSIR-Enhanced EASE-  
786 Grid 2.0 Brightness Temperatures, Version 1, NASA National Snow and Ice Data Center Distributed Active  
787 Archive Center, <https://doi.org/10.5067/QZ3WJNOUZLFK>, 2019.
- 788
- 789 Brodzik, M. J., Billingsley, B., Haran, T., Raup, B., and Savoie, M. H.: EASE-Grid 2.0: Incremental but  
790 significant improvements for Earth-gridded data sets, *ISPRS Int. J. Geo-Inf.*, 1, 32-45,  
791 <https://doi.org/10.3390/ijgi1010032>, 2012.
- 792
- 793 Chu, W., Schroeder, D. M., and Siegfried, M. R.: Retrieval of englacial firn aquifer thickness from ice-  
794 penetrating radar sounding in southeastern Greenland, *Geophys. Res. Lett.*, 45, 11,770-11, 778,  
795 <https://doi.org/10.1029/2018GL079751>, 2018.
- 796
- 797 Chudley, T. R., Christoffersen, P., Doyle, S. H., Bougamont, M., Schoonman, C. M., Hubbard, B., James,  
798 M. R.: Supraglacial lake drainage at a fast-flowing Greenlandic outlet glacier,  
799 *Proc. Natl. Acad. Sci.*, 51, 25468-25477, <https://doi.org/10.1073/pnas.1913685116>, 2019.
- 800
- 801 CReSIS: CReSIS radar depth sounder data, Digital Media, <http://data.cresis.ku.edu/>, 2016.
- 802
- 803 Colgan, W., Rajaram, H., Abdalati, W., McCutchan, C., Mottram, R., Moussavi, M. S., and Grigsby, S.:  
804 Observations, models, and mass balance implications: Glacier crevasses, *Rev. Geophys.*, 54, 119-161,  
805 <https://doi.org/10.1002/2015RG000504>, 2016.



806 Culberg, R., Schroeder, D.M. and Chu, W.: Extreme melt season ice layers reduce firn permeability across  
807 Greenland, *Nat Commun*, 12, 2336, <https://doi.org/10.1038/s41467-021-22656-5>, 2021  
808  
809 Culberg, R.: Refrozen melt layer location, density, and connectivity records from airborne radar sounding,  
810 Greenland, NSF Arctic Data Center, <https://doi.org/10.18739/A2736M33W>, 2021.  
811  
812 Cullather, R. I., Andrews, L. C., Croteau, M. J., Digirolamo, N. E., Hall, D. K., Lim, Y., Loomis, B. D.,  
813 Shuman, C. A., and Nowicki, S. M. J.: Anomalous circulation in July 2019 resulting in mass loss on the  
814 Greenland Ice Sheet. *Geophys. Res. Lett.*, 47, <https://doi.org/10.1029/2020GL087263>, 2020.  
815  
816 Das, S. B., Joughin, I., Behn, M. D., Howat, I. M., King, M. A., Lizarralde, D., Bhatia, M. P., Fracture  
817 propagation to the base of the Greenland Ice Sheet during supraglacial lake drainage, *Science*, 320, 778-  
818 781, <https://doi.org/10.1126/science.1153360>, 2008.  
819  
820 Dunmire, D., Banwell, A. F., Lenaerts, J. T. M., and Datta, R. T.: Contrasting regional variability of buried  
821 meltwater extent over two years across the Greenland Ice Sheet, *The Cryosphere Discuss*,  
822 <https://doi.org/10.5194/tc-2021-3>, in review, 2021.  
823  
824 Early, D. S., and Long, D. G.: Image reconstruction and enhanced-resolution imaging from irregular  
825 samples, *IEEE Trans. Geosci. Remote Sens.* 39, 291-302, <https://doi.org/10.1109/36.905237>, 2001.  
826  
827 Echelmeyer, K., Clarke, T. S., and Harrison, W. D.: Surficial glaciology of Jakobshavn Isbræ, West  
828 Greenland 1. Surface morphology, *J. Glaciol.*, 37, 368–382, <https://doi.org/10.1017/S002214300005803>,  
829 1991.  
830  
831 Entekhabi, D., et al.: The Soil Moisture Active Passive (SMAP) Mission, *Proc. IEEE*, 98, 704-716,  
832 <https://doi.org/10.1109/JPROC.2010.2043918>, 2010.  
833  
834 Forster, R. R., Box, J. E., Van Den Broeke, M. R., Miège, C., Burgess, E. W., Van Angelen, J. H., Lenaerts,  
835 J. T. M., Koenig, L. S., Paden, J., Lewis, C., Gogineni, S. P., Leuschen, C., and McConnell, J. R.: Extensive  
836 liquid meltwater storage in firn within the Greenland Ice Sheet, *Nat. Geosci.*, 7, 95–98,  
837 <https://doi.org/10.1038/ngeo2043>, 2014.  
838  
839 Fountain, A. G., and Walder, J. S.: Water flow through temperate glaciers. *Rev. of Geophys.*, 36, 299-328,  
840 <https://doi.org/10.1029/97RG03579>, 1998.  
841  
842 Freilich, M. H., Long, D. G., and Spencer, M. W.: SeaWinds: A scanning scatterometer for ADEOS-II  
843 science overview, *Proc. IEEE*, 1994, 960-963, <https://doi.org/10.1109/IGARSS.1994.399313>, 1994.  
844  
845 Franco, B., Fettweis, X., and Erpicum, M.: Future projections of the Greenland ice sheet energy balance  
846 driving the surface melt, *The Cryosphere*, 7, 1–18, <https://doi.org/10.5194/tc-7-1-2013>, 2013  
847  
848 Hall, D. K., and DiGirolamo, N.: Multilayer Greenland Ice Surface Temperature, Surface Albedo, and Water  
849 Vapor from MODIS, Version 1, NASA National Snow and Ice Data Center Distributed Active Archive Center,  
850 <https://doi.org/10.5067/7THUWT9NMPDK>, 2019.  
851  
852 Hall, D. K., Comiso, J. C., Digirolamo, N. E., Shuman, C. A., Key, J. R., and Koenig, L. S.: A satellite-derived  
853 climate-quality data record of the clear-sky surface temperature of the Greenland Ice Sheet, *J. Clim.*, 25,  
854 4785–4798, <https://doi.org/10.1175/JCLI-D-11-00365.1>, 2012.  
855  
856 Haran, T., Bohlander J., Scambos T., Painter, T., and Fahnestock, M.: MEaSUREs MODIS Boulder,  
857 Colorado USA. NASA National Snow and Ice Data Center Distributed Active Archive Center,  
858 <https://doi.org/10.5067/9ZO79PHOTYE5>, 2018.  
859

860 Harper, J., Humphrey, N., Pfeffer, W. T., Brown, J., and Fettweis, X.: Greenland ice-sheet contribution to  
861 sea-level rise buffered by meltwater storage in firn, *Nature*, 491, 240–243,  
862 <https://doi.org/10.1038/nature11566>, 2012.  
863  
864 Hicks, B. R., and Long, D. G.: Inferring Greenland melt and refreeze severity from SeaWinds scatterometer  
865 data, *Int. J. Remote Sensing*, 32, 8053-8080, <https://doi.org/10.1080/01431161.2010.532174>, 2011.  
866  
867 Howat, I.: MEaSURES Greenland Ice Mapping Project (GIMP) Land Ice and Ocean Classification Mask,  
868 Version 1, NASA National Snow and Ice Data Center Distributed Active Archive Center,  
869 <https://doi.org/10.5067/B8X58MQBFUPA>, 2017.  
870  
871 Howat, I., Negrete, A., and Smith, B.: MEaSURES Greenland Ice Mapping Project (GIMP) Digital Elevation  
872 Model, Version 1, NASA National Snow and Ice Data Center Distributed Active Archive Center, doi:  
873 <https://doi.org/10.5067/NV34YUIXLP9W>, 2015.  
874  
875 Howat, I., Negrete, A., and Smith, B.: The Greenland Ice Mapping Project (GIMP) land classification and  
876 surface elevation datasets, *The Cryosphere*, 8, 1509-1518, <https://doi.org/10.5194/tc-8-1509-2014>, 2014.  
877  
878 Humphrey, N. F., Harper, J. T., and Pfeffer, W. T.: Thermal tracking of meltwater retention in Greenland's  
879 accumulation area, *J. Geophys. Res.*, 117, <https://doi.org/10.1029/2011JF002083>, 2012.  
880  
881 Jezek, K. C., Gogineni, P., and Shanableh, M.: Radar measurements of melt zones on the Greenland Ice  
882 Sheet, *Geophys. Res. Lett.*, 21, 33-36, <https://doi.org/10.1029/93GL03377>, 1994.  
883  
884 Jezek, K. C., Johnson, J. T., Drinkwater, M. R., Macelloni, G., Tsang, L., Aksoy, M., and Durand M.:  
885 Radiometric approach for estimating relative changes in intraglacier average temperature, *IEEE Trans.*  
886 *Geosci. Remote Sens.*, 53, 134-143, <https://doi.org/10.1109/TGRS.2014.2319265>, 2015.  
887  
888 Jezek, K. C., Johnson J. T., Tan S., Tsang L., Andrews, M. J., Brogioni, M., Macelloni, G., Durand, M.,  
889 Chen, C. C., Belgiovane, D. J., Duan, Y., Yardim, C., Li, H., Bringer, A., Leuski, V., and Aksoy, M.: 500–  
890 2000-MHz brightness temperature spectra of the northwestern Greenland Ice Sheet, *IEEE Trans. Geosci.*  
891 *Remote Sens.*, 56, 1485-1496, <https://doi.org/10.1109/TGRS.2017.2764381>, 2018.  
892  
893 Joughin, I., Das, S. B., Flowers, G. E., Behn, M. D., Alley, R. B., King, M. A., Smith, B. E., Bamber, J. L.,  
894 van den Broeke, M. R., and Van Angelen, J. H.: Influence of ice-sheet geometry and supraglacial lakes on  
895 seasonal ice-flow variability, *The Cryosphere*, 7, 1185-1192, <https://doi.org/10.5194/tc-7-1185-2013>, 2013.  
896  
897 Joughin, I., Das, S. B., King, M. A., Smith, B. E., Howat, I. M., and Moon, T.: Seasonal speedup along the  
898 western flank of the Greenland Ice Sheet, *Science*, 320, 781-783, <https://doi.org/10.1126/science.1153288>,  
899 2008.  
900  
901 Kerr, Y. H., Waldteufel, P., Wigneron, J., Martinuzzi, J., Font, J., and Berger, M.: Soil moisture retrieval from  
902 space: The Soil Moisture and Ocean Salinity (SMOS) mission, *IEEE Trans. Geosci. Remote Sens.*, 39,  
903 1729-1735, <https://doi.org/10.1109/36.942551>, 2001.  
904  
905 Koenig, L. S., Miège, C., Forster, R. R., and Brucker, L.: Initial in situ measurements of perennial meltwater  
906 storage in the Greenland firn aquifer, *Geophys. Res. Lett.*, 41, 81-85,  
907 <https://doi.org/10.1002/2013GL058083>, 2014.  
908  
909 Koenig, L. S., Lampkin, D. J., Montgomery, L. N., Hamilton, S. L., Turrin, J. B., Joseph, C. A., Moutsafa, S.  
910 E., Panzer, B., Casey, K. A., Paden, J. D., Leuschen, C., and Gogineni, P.: Wintertime storage of water in  
911 buried supraglacial lakes across the Greenland Ice Sheet, *The Cryosphere*, 9, 1333–1342,  
912 <https://doi.org/10.5194/tc-9-1333-2015>, 2015.  
913



914 Kuipers Munneke, P. K., Ligtenberg, S. R. M., Van Den Broeke, M. R., Van Angelen, J. H., and Forster, R.  
915 R.: Explaining the presence of perennial liquid water bodies in the firn of the Greenland Ice Sheet, *Geophys.*  
916 *Res. Lett.*, 41, 476–483, <https://doi.org/10.1002/2013GL058389>, 2014.

917

918 Le Vine, D. M., Lagerloef, G. S. E., and Torrusio, S. E.: Aquarius and remote sensing of sea surface salinity  
919 from space, *Proc. IEEE*, 98, 688-703, <https://doi.org/10.1109/JPROC.2010.2040550>, 2010.

920

921 Lewis, C., Gogineni, S., Rodriguez-Morales, F., Panzer, B., Stumpf, T., Paden, J., and Leuschen, C.:  
922 Airborne fine-resolution UHF radar: An approach to the study of englacial reflections, firn compaction and  
923 ice attenuation rates, *J. Glaciology*, 61, 89-100. <https://doi.org/10.3189/2015JoG14J089>, 2015.

924

925 Long, D. G., Brodzik, M. J., and Hardman M. A.: Enhanced-resolution SMAP brightness temperature image  
926 products, *IEEE Trans. Geosci. Remote Sens.*, 57, 4151-4163,  
927 <https://doi.org/10.1109/TGRS.2018.2889427>, 2019.

928

929 Long, D. G., and Brodzik, M. J.: Optimum image formation for spaceborne microwave radiometer products,  
930 *IEEE Trans. Geosci. Remote Sens.*, 54, 2763-2779. <https://doi.org/10.1109/TGRS.2015.2505677>, 2016.

931

932 Long, D. G., and Daum, D. L.: Spatial resolution enhancement of SSM/I data, *IEEE Trans. Geosci. Remote*  
933 *Sens.*, 36, 407-417, <https://doi.org/10.1109/36.662726>, 1998.

934

935 Long, D. G., Hardin, P. J., and Whiting, P. T.: Resolution enhancement of spaceborne scatterometer data,  
936 *IEEE Trans. Geosci. Remote Sens.*, 31, 700-715, <https://doi.org/10.1109/36.225536>, 1993.

937

938 MacFerrin, M., Machguth, H., van As, D., Charalampidis, C., Stevens, C. M., Heilig, A., Vandecrux, B.,  
939 Langen, P. L., Mottram, R., Fettweis, X., van den Broeke, M. R., Pfeffer, W. T., Moussavi, M. S., and  
940 Abdalati, W.: Rapid expansion of Greenland's low-permeability ice slabs. *Nature*, 573, 403-407,  
941 <https://doi.org/10.1038/s41586-019-1550-3>, 2019.

942

943 Machguth, H. MacFerrin M., van As, D., Box, J. E., Charalampidis, C., Colgan., W., Fausto, R. S., Harro,  
944 A. J., Mosley-Thompson, E., and van de Wal, R. S. W.: Greenland meltwater storage in firn limited by  
945 near-surface ice formation. *Nat. Clim. Chang.* 6, 390-393, <https://doi.org/10.1038/nclimate2899>, 2016.

946

947 Mätzler, C., and Hüppi, R.: Review of signature studies for microwave remote sensing of snowpacks, *Adv.*  
948 *in Space Res.*, 9, 253-265, [https://doi.org/10.1016/0273-1177\(89\)90493-6](https://doi.org/10.1016/0273-1177(89)90493-6), 1989.

949

950 Miège, C., Forster, R. R., Brucker, L., Koenig, L. S., Solomon, D.K., Paden, J. D., Box, J. E., Burgess, E.  
951 W., Miller, J. Z., McNerney, L., Brautigam, N., Fausto, R. S., and Gogineni, S.: Spatial extent and temporal  
952 variability of Greenland firn aquifers detected by ground and airborne radars, *J. Geophys. Res. Earth*, 121,  
953 2381–2398, <https://doi.org/10.1002/2016JF003869>, 2016.

954

955 Miles, K. E., Willis, I. C., Benedek, C. L., Williamson, A. G., and Tedesco, M.: Toward monitoring surface  
956 and subsurface lakes on the Greenland Ice Sheet Using Sentinel-1 SAR and Landsat-8 OLI imagery,  
957 *Frontiers in Earth Science*, 5, 58, <https://doi.org/https://doi.org/10.3389/feart.2017.00058>, 2017.

958

959 Miller, J. Z., Long, D. G., Jezek, K. C., Johnson, J. T., Brodzik, M. J., Shuman, C. A., Koenig, L. S., and  
960 Scambos, T. A.: Brief communication: Mapping Greenland's perennial firn aquifers using enhanced-  
961 resolution L-band brightness temperature image time series, *The Cryosphere*, 14, 2809–2817,  
962 <https://doi.org/10.5194/tc-14-2809-2020>, 2020.

963

964 Miller, J. Z.: Mapping Greenland's firn aquifers from space using active and passive satellite microwave  
965 remote sensing, Ph.D. thesis, Department of Geography, University of Utah, 135 pp., 2019.

966

967 Miller, O. L., Solomon, D. K., Miège, C., Koenig, L. S., Forster, R. R., Montgomery, L. N., Schmerr, N.,  
968 Ligtenberg, S. R. M., Legchenko, A., and Brucker, L.: Hydraulic conductivity of a firn aquifer in southeast  
969 Greenland, *Front. Earth Sci.*, 5, <https://doi.org/10.3389/feart.2017.00038>, 2017.

970 Montgomery, L. N., Schmerr, N., Burdick, S., Forster, R. R., Koenig, L., Legchenko, A., Ligtenberg, S.,  
971 Miège, C., Miller, O. L., and Solomon, D. K.: Investigation of firn aquifer structure in southeastern Greenland  
972 using active source seismology, *Front. Earth Sci.*, 5, <https://doi.org/10.3389/feart.2017.00010>, 2017.  
973

974 Moon, T., Joughin, I., Smith, B., Broeke, M. R., Berg, W. J., Noël, B., and Usher, M.: Distinct patterns of  
975 seasonal Greenland glacier velocity, *Geophys. Res. Lett.*, 41, 7209-7216,  
976 <https://doi.org/10.1002/2014GL061836>, 2014.  
977

978 Mote, T. L., and Andersen, M. R.: Variations in snowpack melt on the Greenland Ice Sheet based on passive  
979 microwave measurements, *J. Glaciology*, 41, 51-60, <https://doi.org/10.1017/S002214300017755>, 1995.  
980 Müller, F.: Zonation in the Accumulation Area of the Glaciers of Axel Heiberg Island, N.W.T., Canada, *J. of*  
981 *Glaciology*, 4, 302-311, 1962.  
982

983 Noël, B., van Kampenhout, L., Lenaerts, J. T. M., van de Berg, W. J, and van den Broeke, M. R.: A 21st  
984 century warming threshold for sustained Greenland Ice Sheet mass loss, *Geophys. Res. Lett.*, 48(5),  
985 <https://doi.org/10.1029/2020GL090471>, 2021.  
986

987 Noël, B., van de Berg, Willem Jan, Lhermitte, S. L. M., and van den Broeke, Michiel R.: Rapid ablation zone  
988 expansion amplifies north Greenland mass loss, *Sci. Adv.*, 5, eaaw0123,  
989 <https://doi.org/10.1126/sciadv.aaw0123>, 2019.  
990

991 Nghiem, S.V., Steffen, K., Neumann, G.A., and Huff, R: Mapping of ice layer extent and snow accumulation  
992 in the percolation zone of the Greenland ice sheet, *J. Geophys. Res.*, 110,  
993 <https://agupubs.onlinelibrary.wiley.com/doi/full/10.1029/2004JF000234>. 2005.  
994

995 Nghiem, S. V., Hall, D. K., Mote, T. L., Tedesco, M., Albert, M. R., Keegan, K., Shuman, C. A., DiGirolamo,  
996 N.E., and Neumann, G.: The extreme melt across the Greenland Ice Sheet in 2012, *Geophys. Res. Lett.*,  
997 39, L20502, <https://doi.org/10.1029/2012GL053611>, 2012.  
998

999 Paden, J., Li, J., Leuschen C., F. Rodriguez-Morales, F., and Hale, R.: IceBridge Accumulation Radar L1B  
1000 Geolocated Radar Echo Strength Profiles, Version 2, NASA National Snow and Ice Data Center Distributed  
1001 Active Archive Center, <https://doi.org/10.5067/OZY1XYHNIQNY>, 2014, updated 2018.  
1002

1003 Pfeffer, W. T., Meier, M. F., and Illangasekare, T. H.: Retention of Greenland runoff by refreezing:  
1004 Implications for projected future sea level change. *J. Geophys. Res. Oceans*, 96, 22117-22124,  
1005 <https://doi.org/10.1029/91JC0250>, 1991.  
1006

1007 Pfeffer, W. T., and Humphrey, N.F.: Determination of timing and location of water movement and ice-layer  
1008 formation by temperature measurements in sub-freezing snow, *J. Glaciol.*, 42, 292-304,  
1009 <https://doi.org/10.1017/S002214300004159>, 1996.  
1010

1011 Piepmeier, J. R., et al.: SMAP L-band microwave radiometer: Instrument design and first year on orbit.  
1012 *IEEE Trans. Geosci. Remote Sens*, 55, 1954-1966, <https://doi.org/10.1109/TGRS.2016.2631978>, 2017.  
1013

1014 Poinar, K., Joughin, I., Lilien, D., Brucker, L., Kehrl, L., and Nowicki, S.: Drainage of southeast Greenland  
1015 firn aquifer water through crevasses to the bed. *Front. Earth Sci.*, <https://doi.org/10.3389/feart.2017.00005>,  
1016 2017.  
1017

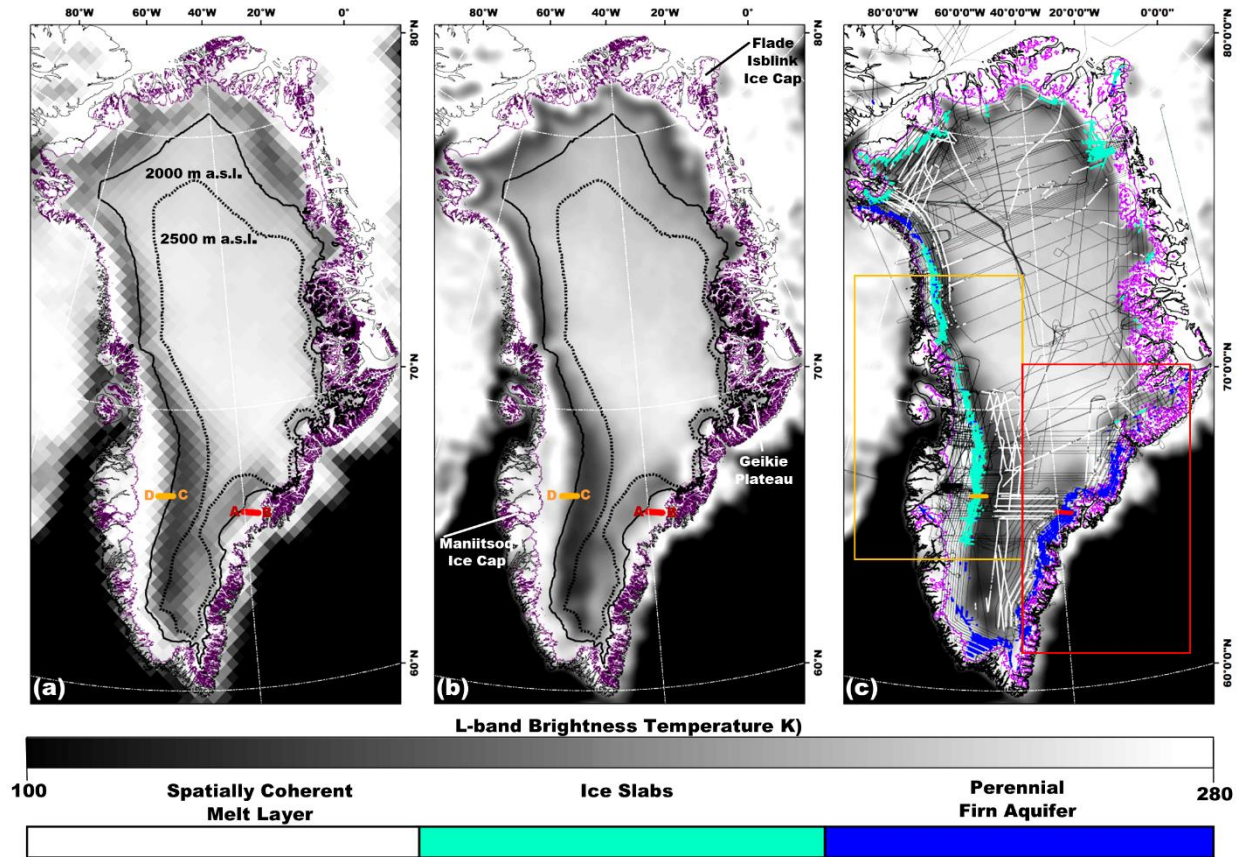
1018 Poinar, K., Dow, C. F., and Andrews, L. C.: Long-term support of an active subglacial hydrologic system in  
1019 southeast Greenland by firn aquifers. *Geophys. Res. Lett.*, 46, 4772-4781,  
1020 <https://doi.org/10.1029/2019GL082786>, 2019.  
1021

1022 Rignot, E.: Backscatter model for the unusual radar properties of the Greenland Ice Sheet, *J. Geophys.*  
1023 *Res. Planets*, 100, 9389–9400, <https://doi.org/10.1029/95JE00485>, 1995.  
1024

1025 Rignot, E. J., Ostro, S. J., Van Zyl, J., and Jezek, K. C.: Unusual radar echoes from the Greenland Ice  
1026 Sheet, *Science*, 261, 1710-1713, <https://doi.org/10.1126/science.261.5129.171>, 1993.  
1027  
1028 Rodriguez-Morales, F., et al.: Advanced multi-frequency radar instrumentation for polar research, *IEEE*  
1029 *Trans. Geosci. Remote Sens.*, 52, 2824-2842, <https://doi.org/10.1109/TGRS.2013.2266415>, (2014).  
1030  
1031 Schröder L., Neckel N., Zindler R., Humbert A.: Perennial supraglacial lakes in northeast Greenland  
1032 observed by polarimetric SAR, *Remote Sensing*, 12, 2798, <https://doi.org/10.3390/rs12172798> (2020).  
1033  
1034 Shuman, C. A., Hall, D. K., DiGirolamo, N. E., Mefford T. K., and Schnaubelt, M. J.: Comparison of near-  
1035 surface air temperatures and MODIS ice-surface temperatures at Summit, Greenland (2008–2013), *J. Appl.*  
1036 *Meteor. Climatol.*, 53, 2171-2180, <https://doi.org/10.1175/JAMC-D-14-0023.1>, 2014.  
1037  
1038 Steffen, K., Nghiem, S. V., Huff, R., and Neumann, G.: The melt anomaly of 2002 on the Greenland Ice  
1039 Sheet from active and passive microwave satellite observations. *Geophys. Res. Lett.*, 31, L2040,  
1040 <https://doi.org/10.1029/2004GL020444>, 2004.  
1041  
1042 Stevens, L. A., Behn, M. D., McGuire, J. J., Das, S. B., Joughin, I., Herring, T., Shean, D. E., and King, M.  
1043 A.: Greenland supraglacial lake drainages triggered by hydrologically induced basal slip, *Nature*, 522, 73-  
1044 76. <https://doi.org/10.1038/nature14480>, 2015.  
1045  
1046 Swift, C. T., Hayes, P. S., Herd, J. S., Jones, W. L., and Delnore, V. E.: Airborne microwave measurements  
1047 of the southern Greenland Ice Sheet, *J. Geophys. Res. Solid Earth*, 90, 1983-1994,  
1048 <https://doi.org/10.1029/JB090iB02p01983>, 1985.  
1049  
1050 Tedesco, M., and Fettweis, X.: Unprecedented atmospheric conditions (1948–2019) drive the 2019  
1051 exceptional melting season over the Greenland Ice Sheet, *The Cryosphere*, 14, 1209-1223,  
1052 <https://doi.org/10.5194/tc-14-1209-2020>, 2020.  
1053  
1054 Tedesco, M., Mote, T., Fettweis, X., Hanna, E., Jeyaratnam, J., Booth, J. F., Datta, R., and Briggs, K.: Arctic  
1055 cut-off high drives the poleward shift of a new Greenland melting record, *Nature Commun.*, 7, 11723-11723,  
1056 <https://doi.org/10.1038/ncomms11723> 1985, 2016.  
1057  
1058 Tedesco, M., Fettweis, X., van den Broeke, M. R., van de Wal, R. S. W., Smeets, C. J. P. P., van de Berg,  
1059 W. J., Serreze, M. C., and Box, J. E.: The role of albedo and accumulation in the 2010 melting record in  
1060 Greenland, *Environ. Res. Lett.* 6, 014005, <https://doi.org/10.1088/1748-9326/6/1/014005>, 2011.  
1061  
1062 Tedesco, M., Serreze, M., and Fettweis, X.: Diagnosing the extreme surface melt event over southwestern  
1063 Greenland in 2007. *The Cryosphere*, 2, 159-166. <https://doi.org/10.5194/tc-2-159-2008>, 2008.  
1064  
1065 Tiuri, M. E., Sihvola, A. H., Nyfors, E. G., Hallikaiken, M. T.: The complex dielectric constant of snow at  
1066 microwave frequencies, *IEEE J. Ocean Eng.* 9, 377-382, <https://doi.org/10.1109/JOE.1984.1145645>, 1984.  
1067  
1068 Tsai, W., Nghiem, S. V., Van Zyl, J. J.: SeaWinds scatterometer on QuikSCAT mission and the emerging  
1069 land and ocean applications, *Proc. SPIE* 4152, <https://doi.org/10.1117/12.410586>, 2000.  
1070  
1071 Turton, J. V., Hochreuther, P., Reimann, N., and Blau, M. T.: The distribution and evolution of supraglacial  
1072 lakes on the 79° N Glacier (northeast Greenland) and interannual climatic controls, *The Cryosphere*  
1073 *Discuss.* <https://doi.org/10.5194/tc-2021-45>, in review, 2021.  
1074  
1075 Ulaby, F. T., Long, D. G., Blackwell, W. J., Elachi, C., Fung, A. K., Ruf, C., Sarabandi, C., Zebker, H. A.,  
1076 Van Zyl, J.: *Microwave radar and radiometric remote sensing*, University of Michigan Press, Ann Arbor,  
1077 2014.  
1078

1079 van den Broeke, M. R., Enderlin, E. M., Howat, I. M., Kuipers Munneke, P., Noël, B. P. Y., van de Berg, W.  
1080 J., van Meijgaard, E., and Wouters, B.: On the recent contribution of the Greenland ice sheet to sea level  
1081 change, *The Cryosphere*, 10, 1933–1946, <https://doi.org/10.5194/tc-10-1933-2016>, 2016.  
1082  
1083 van der Veen, C. J.: Fracture propagation as means of rapidly transferring surface meltwater to the base  
1084 of glaciers, *Geophys. Res. Lett.*, 34, L01501, <https://doi.org/10.1029/2006GL028385>, 2005.  
1085  
1086 Wessel, P., and Smith, W. H. F.: A global, self-consistent, hierarchical, high-resolution shoreline database,  
1087 *J. Geophys. Res.*, 101, 8741–8743, <https://doi.org/10.1029/96JB00104>, 1996.  
1088  
1089 Zwally, H. J., Abdalati, W., Herring, T., Larson, K., Saba, J., and Steffen, K.: Surface melt-induced  
1090 acceleration of Greenland Ice Sheet flow, *Science*, 297, 218-222, <https://doi.org/10.1126/science.1072708>,  
1091 2002.  
1092  
1093 Zwally, J. H.: Microwave emissivity and accumulation rate of polar firn, *J. Glaciol.*, 18, 195-215,  
1094 <https://doi.org/10.1017/S0022143000021304>, 1977.  
1095  
1096

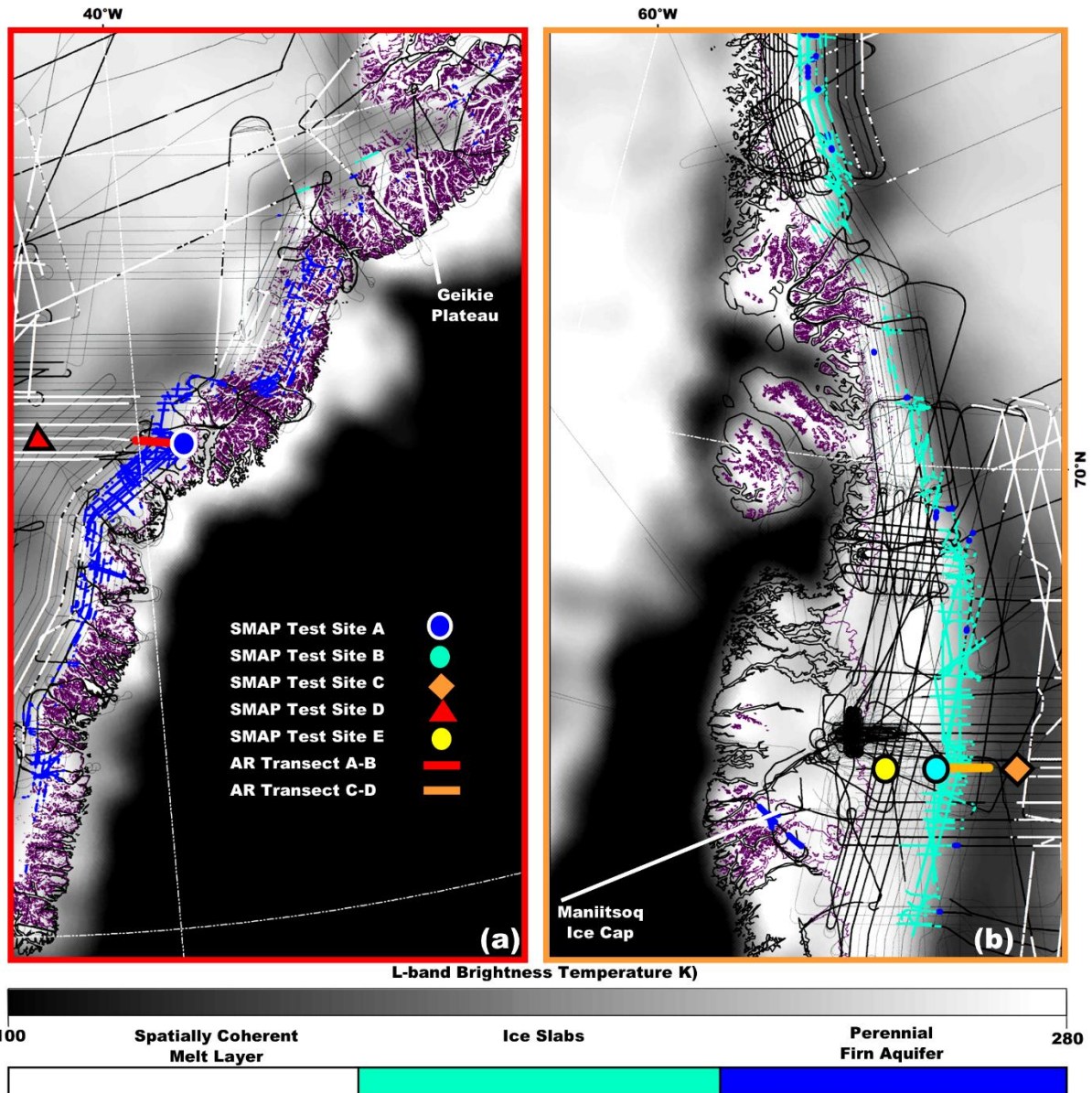




1097

1098 **Figure 1**

1099 (a) Gridded (25 km gridding, 30 km effective resolution), and (b) enhanced-resolution (3.125 km gridding,  
 1100 18 km effective resolution) L-band  $T_V^B$  imagery generated using observations collected 15 April 2016 by the  
 1101 microwave radiometer on the SMAP satellite during the evening orbital pass interval over Greenland (Long  
 1102 et al., 2019) overlaid with the 2000 m a.s.l. contour (black line), and the 2500 m a.s.l. contour (dotted black  
 1103 line; Howat et al., 2014); the ice sheet extent (purple line; Howat et al., 2014); and the coastline (black  
 1104 peripheral line; Wessel and Smith, 1996). (c) SMAP enhanced-resolution L-band  $T_V^B$  imagery overlaid with  
 1105 AR- and MCoRDS-derived 2010-2017 perennial firn aquifer (blue shading; Miège et al., 2016), 2010-2014  
 1106 ice slab (cyan shading; MacFerrin et al., 2019), and 2012 spatially coherent melt layer (white shading;  
 1107 Culberg et al., 2021) detections along OIB flight lines (black interior lines); zoom areas over south eastern  
 1108 Greenland (red box; Fig. 2a), and south western Greenland (orange box; Fig. 2b); and AR radargram  
 1109 transect A-B (red line; Fig. 3a) and C-D (orange line; Fig. 3b).

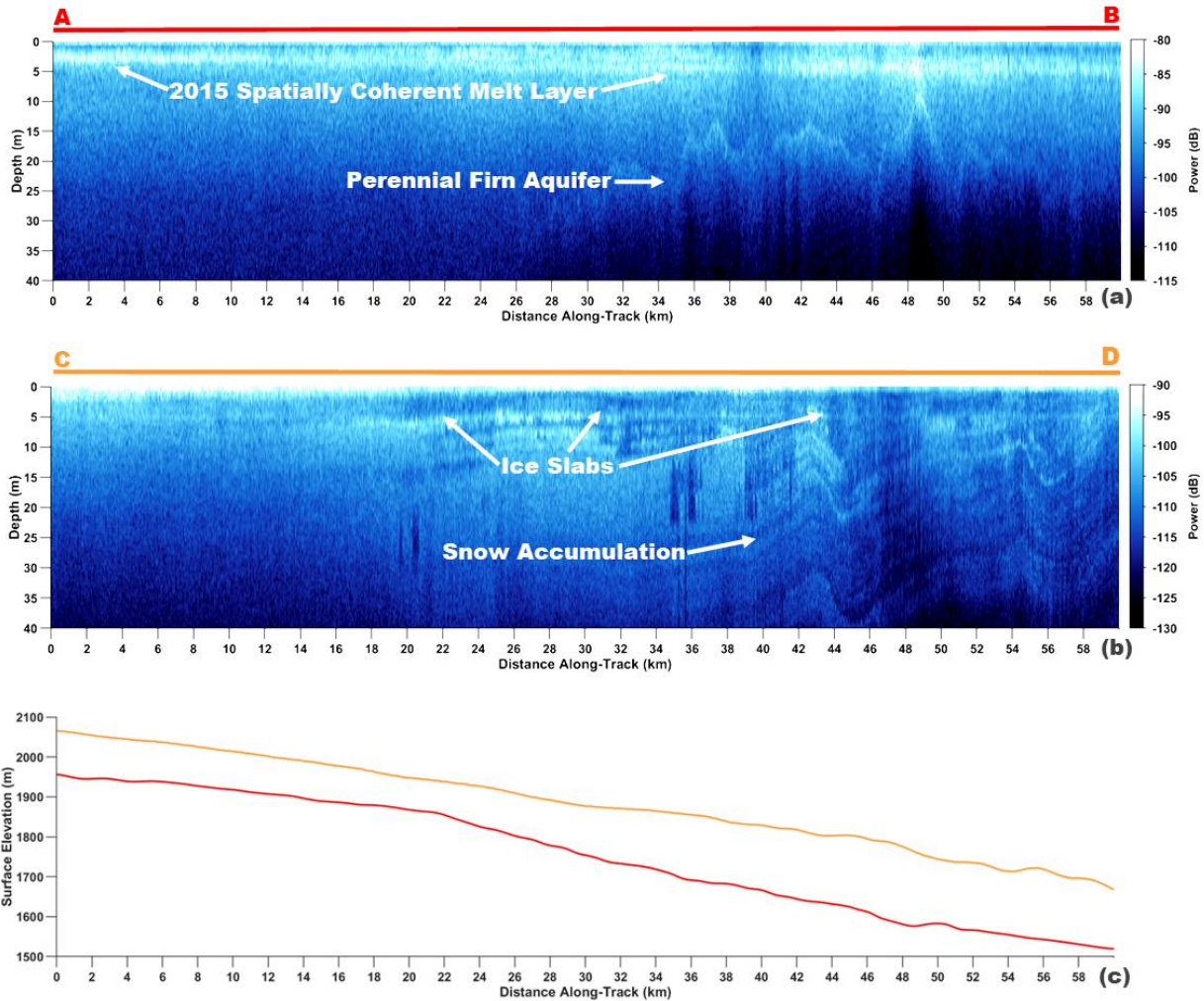


1110

1111 **Figure 2**

1112 *Enhanced-resolution (3.125 km gridding, 30 km effective resolution) L-band  $T_v^B$  imagery generated using*  
 1113 *observations collected 15 April 2016 by the microwave radiometer on the SMAP satellite during the evening*  
 1114 *orbital pass interval over (a) south eastern Greenland (red box, Fig. 1c), and (b) south western Greenland*  
 1115 *(orange box, Fig. 1c,) (Long et al., 2019) overlaid with the ice sheet extent (purple line; Howat et al., 2014);*  
 1116 *the coastline (black peripheral line; Wessel and Smith, 1996); the AR- and MCoRDS-derived 2010-2017*  
 1117 *perennial firn aquifer (blue shading; Miège et al., 2016), 2010-2014 ice slab (cyan shading; MacFerrin et*  
 1118 *al., 2019), and 2012 spatially coherent melt layer (white shading; Culberg et al., 2021) detections along OIB*  
 1119 *flight lines (black interior lines); AR radargram transect A-B (red line; Fig. 3a), and C-D (orange line; Fig.*  
 1120 *3b); and SMAP Test Site A (blue circle; Fig. 4a), B (cyan circle; Fig. 4b), C (orange diamond; Fig. 4c), D*  
 1121 *(red triangle; Fig. 4d), and E (yellow circle; Fig. 4e).*





1122

1123

**Figure 3**

1124

AR *radargram* transect (a) A-B (red line, Fig. 2a) collected on 22 April 2017, and (b) C-D (orange line, Fig.

1125

2b) collected on 5 May 2017 (Rodriguez-Morales et al, 2014). (c) AR *radargram* transect A-B (red line), and

1126

C-D (orange line) elevation profiles. The exceptionally bright upper surface-parallel reflector in (a) is a

1127

spatially coherent melt layer. The bright lower reflector in (a) is the upper surface of meltwater stored within

1128

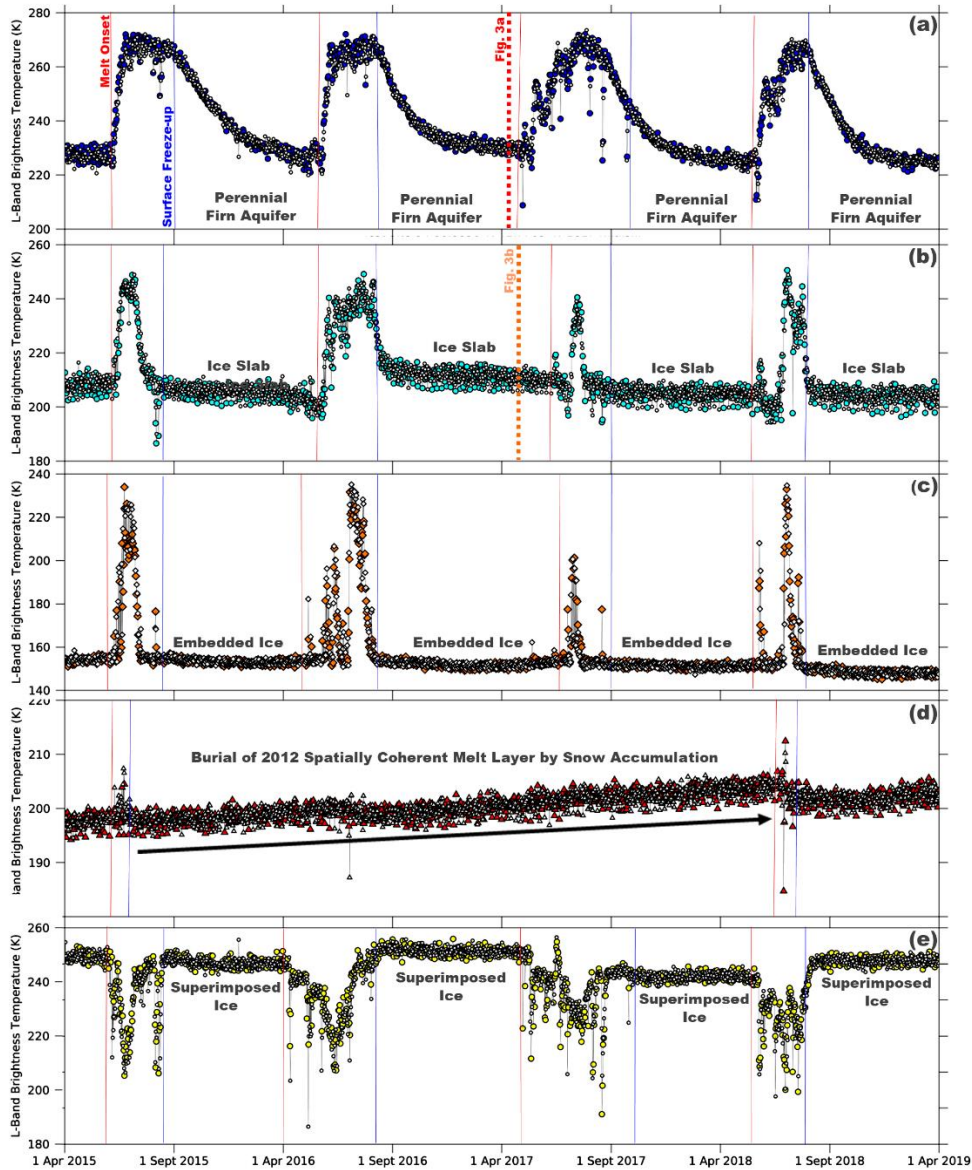
a perennial firn aquifer. The thick dark surface-parallel regions of low-reflectivity in (b) are ice slabs. The

1129

alternating sequences of bright and dark surface-parallel reflectors in (b) are seasonal snow accumulation

1130

layers.

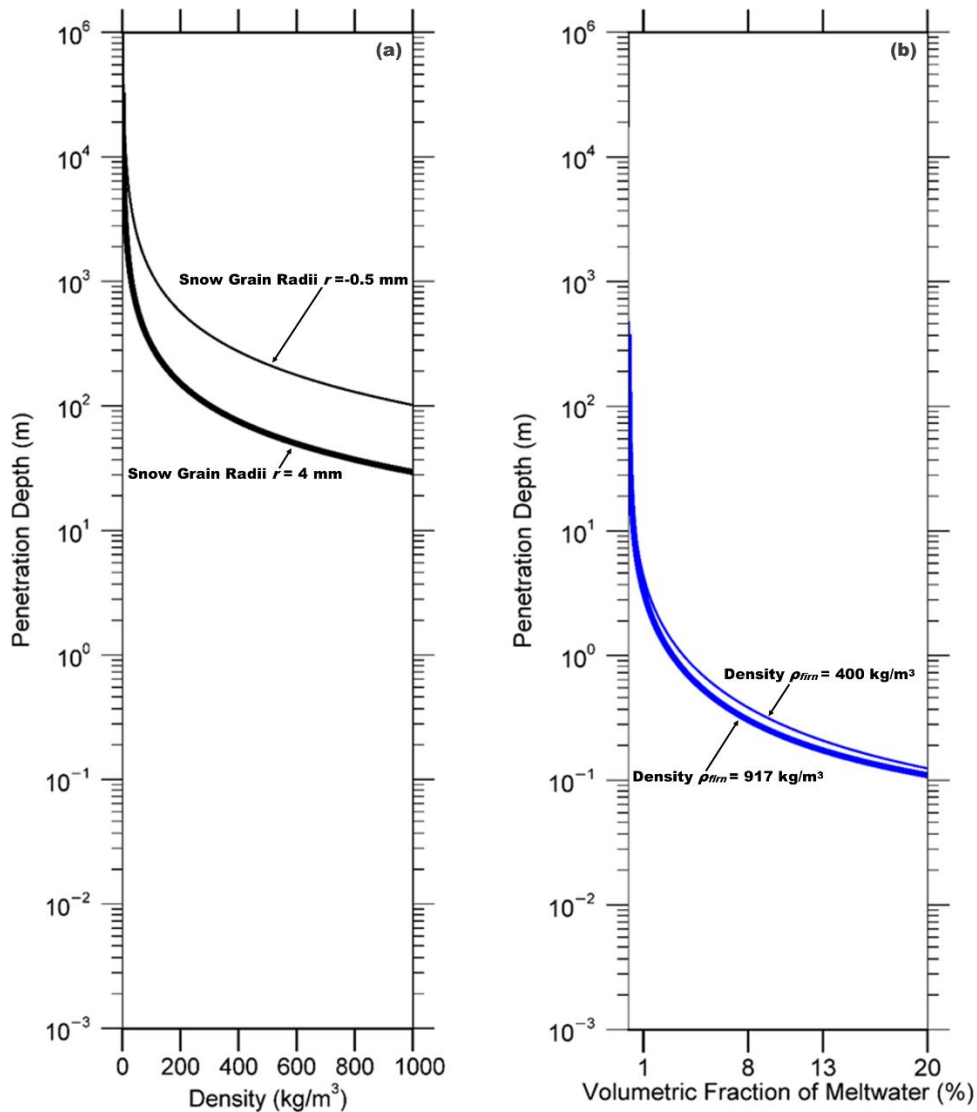


1131

1132 **Figure 4**

1133 *Temporal L-band signatures that alternate morning (white symbols) and evening (colored symbols) orbital*  
 1134 *pass interval enhanced-resolution  $T_V^B$  generated using observations collected over the GRIS by the*  
 1135 *microwave radiometer on the SMAP satellite (Long et al., 2019) over (a) SMAP Test Site A (blue circles;*  
 1136 *Fig. 2a), (b) B (cyan circles; Fig. 2b), (c) C (orange diamonds; Fig. 2b), (d) D (red triangles; Fig. 2a), and (e)*  
 1137 *E (yellow circles; Fig. 2b). Melt onset (red lines) and surface freeze-up (blue lines) dates derived from*  
 1138 *thermal infrared  $T^B$  collected by MODIS on the Terra and Aqua satellites (Hall et al, 2012). AR [radargram](#)*  
 1139 *transect A-B (red dashed line; Figs. 3a) collected on 22 April 2017, and C-D (orange dashed line; Fig. 3b)*  
 1140 *collected on 5 May 2017.*





1141

1142 **Figure 5**

1143 *Theoretical L-band penetration depths for of uniform layer of (a) refrozen, and (b) water-saturated firn.*

1144 *Penetration depths  $\left(\frac{1}{\kappa_s + \kappa_a}\right)$  are calculated as a function of the Raleigh scattering coefficient ( $\kappa_s$ ; Eq. 8), and*

1145 *the absorption coefficient ( $\kappa_a$ ; Eq. 10). The complex dielectric constant is calculated using the empirically*

1146 *derived models described in Tiuri et al., (1984). Refrozen firn penetration depths are calculated as a function*

1147 *of firn density ( $\rho_{firn}$ ), and the curves are plotted for snow grain radii ( $r$ ) set to  $r=0.5$  mm (upper curve), and*

1148  *$r=4$  mm (lower curve). Water-saturated firn penetration depths are calculated as a function of the volumetric*

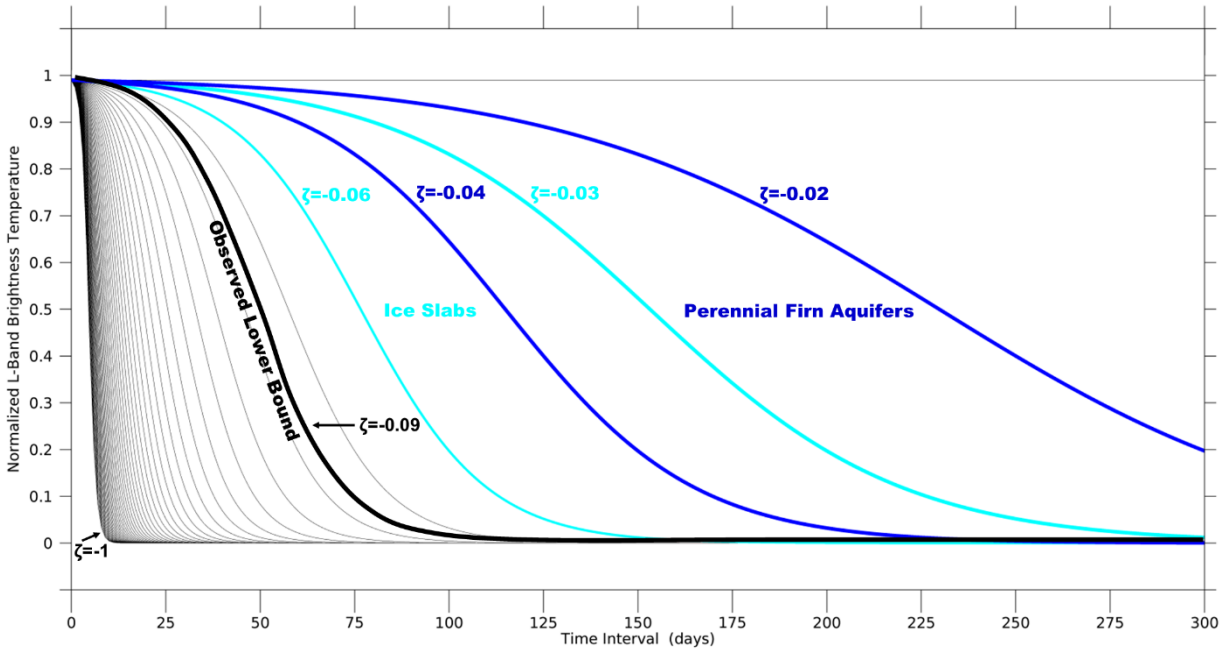
1149 *fraction of meltwater ( $m_v$ ), and the curves are plotted for firn density set to  $\rho_{firn}=400$  kg/m<sup>3</sup> (upper curve),*

1150 *and  $\rho_{firn}=917$  kg/m<sup>3</sup> (lower curve). Given the complexity of modeling embedded ice structures, they are*

1151 *excluded from the penetration depth calculation. Increases in the volumetric fraction of embedded ice within*

1152 *the firn will result in an increase in volume scattering, which will decrease and compress the distance*

1153 *between the penetration depth curves for both refrozen and water-saturated firn.*

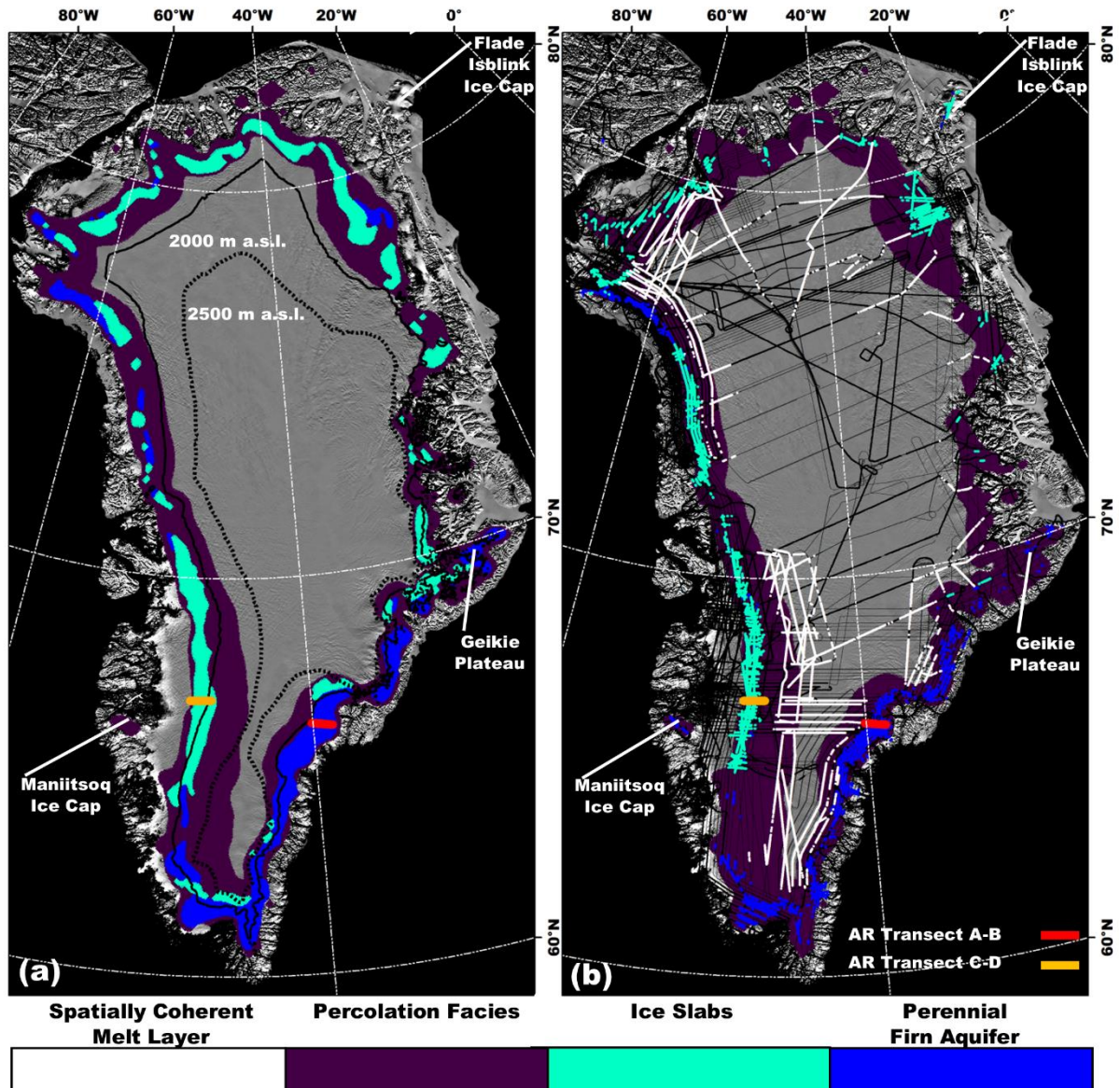


1154

1155 **Figure 6**

1156 *Example set of simulated sigmoidal curves that represent our model of the exponentially*  
 1157 *decreasing temporal L-band signatures predicted over the percolation facies. The initial*  
 1158 *normalized vertically-polarized L-band brightness temperature was fixed at a value of  $T_{V,N}^B(t_{max})$*   
 1159 *= 0.99, and the time interval was set to a value of  $t \in [t_{max}, t_{min}] = 300$  observations. The*  
 1160 *refreezing rate parameter was set to values between  $\zeta = [-1, 0]$  incremented by steps of 0.02.*  
 1161 *The blue lines correspond to the interval  $\zeta \in [-0.04, -0.02]$  and produce curves similar to those*  
 1162 *observed over perennial firn aquifer areas. The cyan lines correspond to the interval  $\zeta \in [-0.06, -$*   
 1163 *0.03] and produce curves similar to those observed over ice slab areas. The black line is the*  
 1164 *observed lower bound ( $\zeta = -0.09$ ) of the refreezing rate parameter of partitioned  $T_V^B$  time series*  
 1165 *iteratively fit to the sigmoid function (Section 2.3.4).*

1166



1168

1169

**Figure 7**

1170 (a) SMAP-derived perennal firn aquifer (blue shading), ice slab (cyan shading), and percolation facies

1171 (purple shading) extents (2015-2019) generated by the adapted empirical algorithm; and the 2000 m a.s.l.

1172 contour (black line), and the 2500 m a.s.l. contour (black dotted line; Howat et al., 2014) overlaid on the

1173 2015 MODIS Mosaic of Greenland (MOG) image map (Haran et al., 2018). (b) SMAP-derived extents are

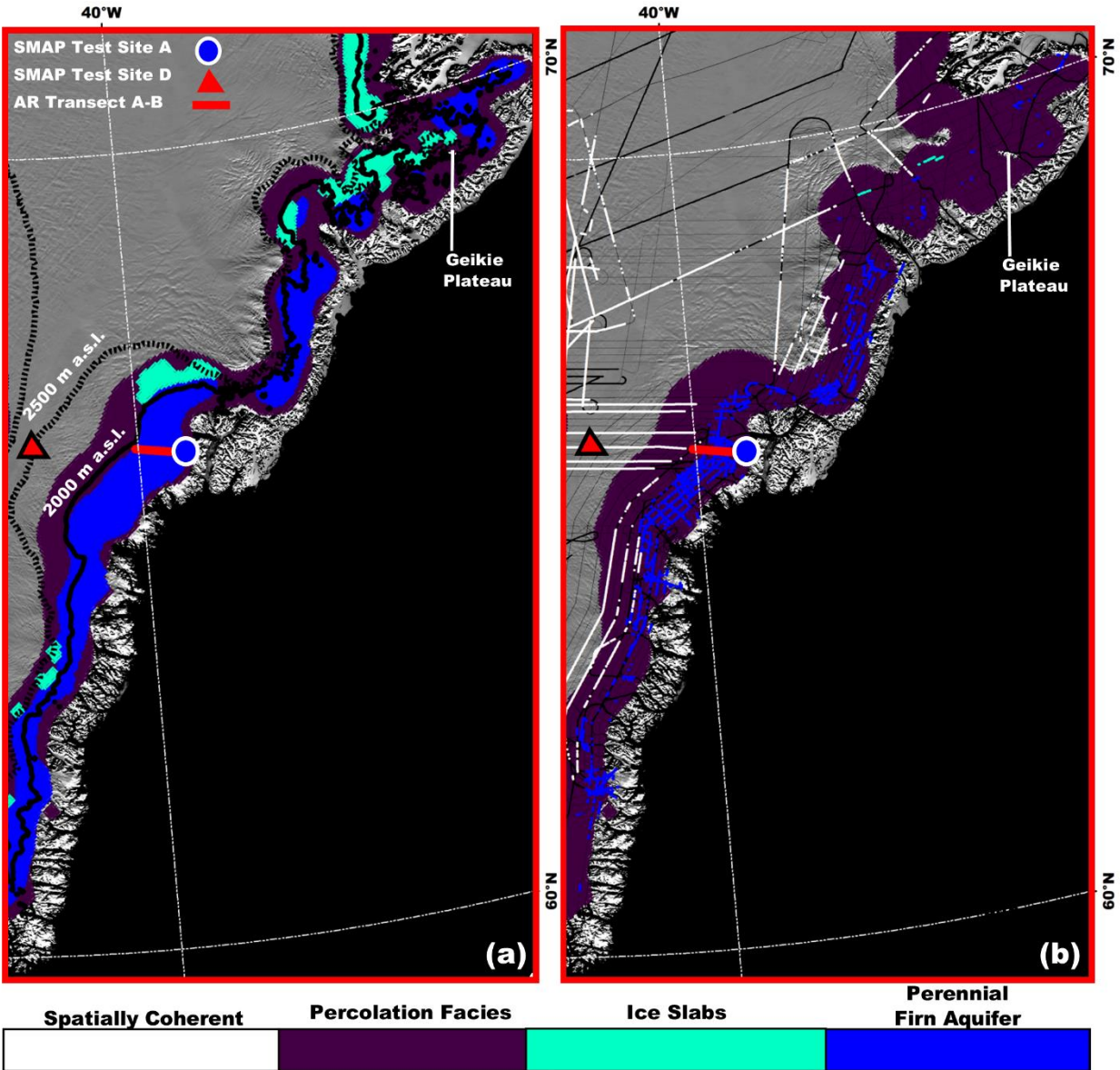
1174 overlaid with AR- and MCoRDS-derived 2010-2017 perennal firn aquifer (blue shading; Miège et al., 2016),

1175 2010-2014 ice slab (cyan shading; MacFerrin et al., 2019), and 2012 spatially coherent melt layer (white

1176 shading; Culberg et al., 2021) detections along OIB flight lines (black interior lines); and AR radargram

1177 transect A-B (red line; Fig. 3a), and C-D (orange line; Fig. 3b).





1178

1179

**Figure 8**

1180

The SMAP-derived perennial firn aquifer (blue shading), ice slab (cyan shading), and percolation facies

1181

(purple shading) extents (2015-2019) generated by the adapted empirical algorithm over south eastern

1182

Greenland (red box; Fig. 1c); and the 2000 m a.s.l. contour (black line), and the 2500 m a.s.l. contour (black

1183

dotted line; Howat et al., 2014) overlaid on the 2015 MODIS MOG image map (Haran et al., 2018). (b) The

1184

SMAP-derived percolation facies extent is overlaid with AR- and MCoRDS-derived 2010-2017 perennial

1185

firn aquifer (blue shading; Miège et al., 2016), 2010-2014 ice slab (cyan shading; MacFerrin et al., 2019),

1186

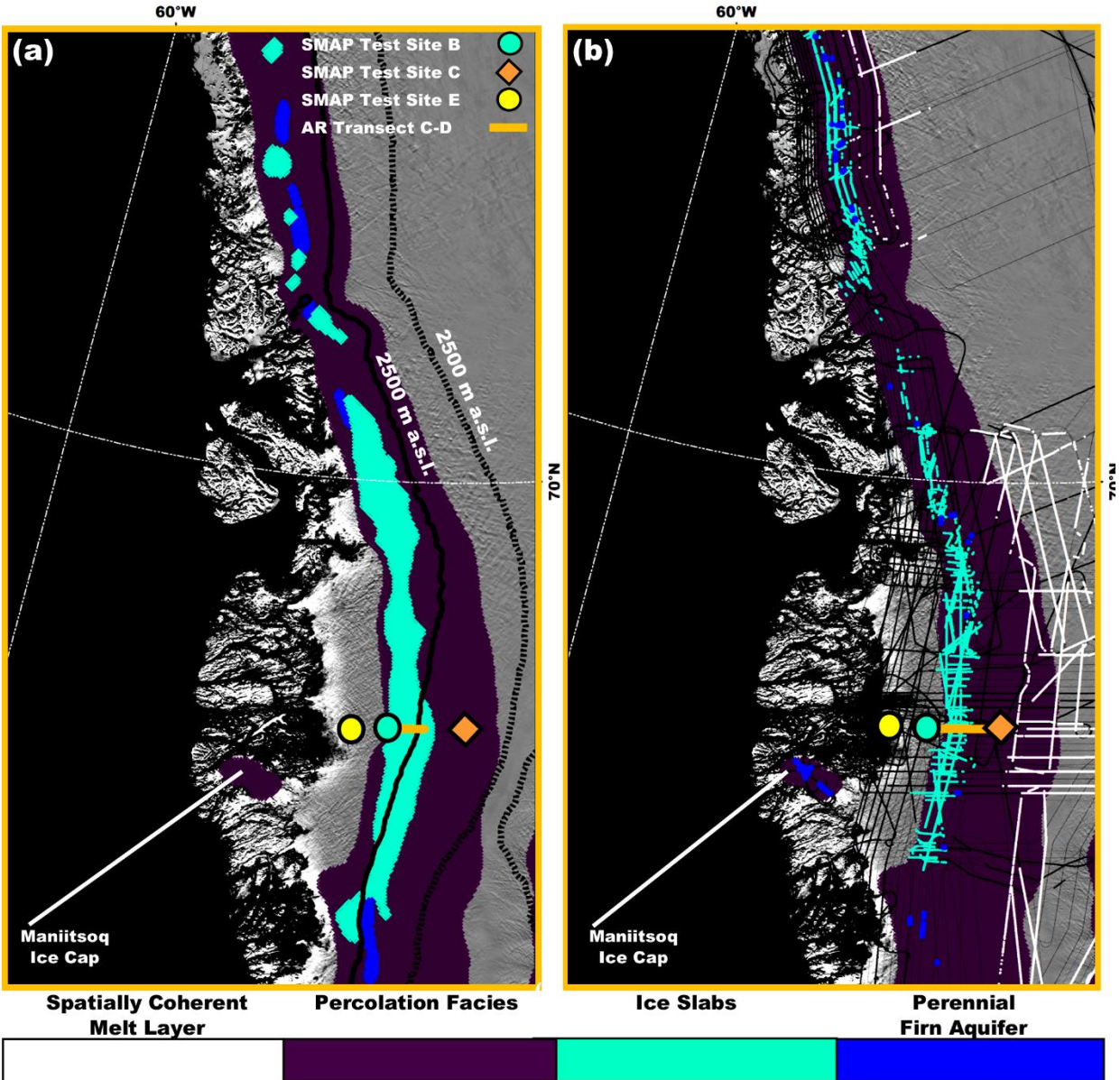
and 2012 spatially coherent melt layer (white shading; Culberg et al., 2021) detections along OIB flight lines

1187

(black lines); AR radargram transect A-B (red line; Fig. 3a); and SMAP Test Site A (blue circle; Fig. 4a),

1188

and D (red triangle; Fig 4d).



1189

1190

**Figure 9**

1191

(a) SMAP-derived perennial firn aquifer (blue shading), ice slab (cyan shading), and percolation facies

1192

(purple shading) extents (2015-2019) generated by the adapted empirical algorithm over south western

1193

Greenland (orange box; Fig. 1c); and the 2000 m a.s.l. contour (black line), and the 2500 m a.s.l. contour

1194

(black dotted line; Howat et al., 2014) overlaid on the 2015 MODIS MOG image map (Haran et al., 2018).

1195

(b) SMAP-derived percolation facies extent is overlaid with AR- and MCoRDS-derived 2010-2017 perennial

1196

firn aquifer (blue shading; Miège et al., 2016), 2010-2014 ice slab (cyan shading; MacFerrin et al., 2019),

1197

and 2012 spatially coherent melt layer (white shading; Culberg et al., 2021) detections along OIB flight lines

1198

(black interior lines); AR *radargram* transect C-D (orange line; Fig. 3b); and SMAP Test Site B (cyan circle;

1199

Fig. 4b), C (orange diamond; Fig. 4c), and E (yellow circle; Fig. 4e).

1200

1201 **Table 1.**

1202 *MODIS-derived total number of days in the melting and freezing seasons; SMAP-derived maximum*  
 1203 *vertically-polarized L-band brightness temperature ( $T_{V,max}^B$ ); minimum vertically-polarized L-band brightness*  
 1204 *temperature ( $T_{V,min}^B$ ); time scale scales of exponential decrease following the surface freeze-up date for*  
 1205 *perennial firn aquifer, ice slab, percolation facies, dry snow facies, and wet snow facies areas.*

	<b>Melting Season (days)</b>	<b>Freezing Season (days)</b>	<b><math>T_{V,max}^B</math> (K)</b>	<b><math>T_{V,min}^B</math> (K)</b>	<b>Exponential Decrease (time scale)</b>
<b>Perennial Firn Aquifers</b>	75 - 100	265 - 290	200 - 275	180 – 250	weeks – months
<b>Ice Slabs</b>	60 -90	275 - 305	170 - 260	130 – 240	days - weeks
<b>Percolation Facies</b>	1 - 60	305 - 364	150 - 200	130 – 220	days
<b>Dry Snow Facies</b>	-	365	200 - 240	200 – 240	-
<b>Wet Snow Facies</b>	90 - 120	245 - 275	230 - 250	230 – 250	-

1206

1207 **Table 2.**

1208 *SMAP-derived calibration parameter intervals used for mapping perennial firn aquifer and ice slab extents.*

	$\xi$	$T_{V,max}^B$ (K)	$T_{V,min}^B$ (K)	$\zeta$
<b>Perennial Firn Aquifers</b>	0.2 – <u>2.84</u>	200 – 275	180 – 250	-0.04 – -0.02
<b>Ice Slabs</b>	0.1 – 2	170 – 260	130 – 240	-0.06 – -0.03

1209

1210 **Table 3.**

1211 *Interannual variability in SMAP-derived perennial firn aquifer and ice slab extents.*

	<b>Perennial Firn Aquifers (km<sup>2</sup>)</b>	<b>Ice Slabs (km<sup>2</sup>)</b>
<b>2015-2019</b>	66,000	76,000
<b>2015-2016</b>	63,000	23,000
<b>2016-2017</b>	69,000	48,000
<b>2017-2018</b>	73,000	27,000
<b>2018-2019</b>	70,000	38,000

1212